Article

Current Biology

Active nuclear positioning and actomyosin contractility maintain leader cell integrity during gonadogenesis

Graphical abstract

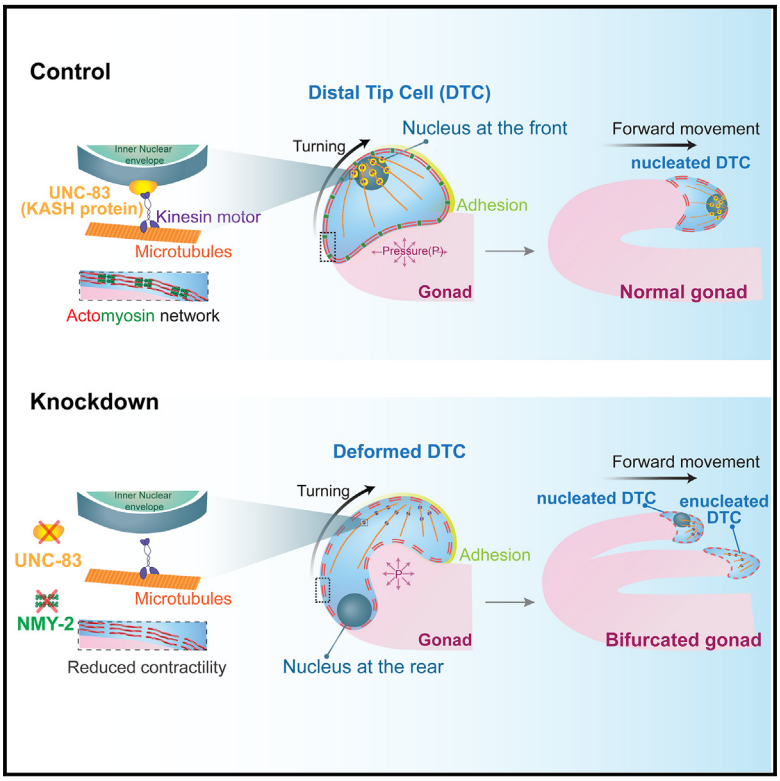

Highlights

- LINC complex protein UNC-83 and kinesin motor position nucleus at the DTC forefront
- Misplaced nucleus and low contractility cause DTC deformation during gonadal turn
- Excessive strain during the turn leads to DTC fragmentation and gonad bifurcation
- Enucleated DTC can invade but does not retain stem cell niche function for long

Authors

Priti Agarwal, Simon Berger, Tom Shemesh, Ronen Zaidel-Bar

Correspondence

pritiag007@gmail.com (P.A.), zaidelbar@tauex.tau.ac.il (R.Z.-B.)

In brief

Agarwal et al. combine cell-specific knockdown, long-term imaging, and physical modeling to show that the leader distal tip cell (DTC) employs two complementary mechanical strategies, active nuclear positioning by microtubule motors and actomyosin-driven cortical contractility, to prevent its deformation and ensure normal *C. elegans* gonadogenesis.

Agarwal et al., 2024, Current Biology *34*, 1–14
June 3, 2024
https://doi.org/10.1016/j.cub.2024.03.049

CellPress

Please cite this article in press as: Agarwal et al., Active nuclear positioning and actomyosin contractility maintain leader cell integrity during gonadogenesis, Current Biology (2024), https://doi.org/10.1016/j.cub.2024.03.049

Current Biology

CellPress

Article

Active nuclear positioning and actomyosin contractility maintain leader cell integrity during gonadogenesis

Priti Agarwal,[1,*] Simon Berger,[2] Tom Shemesh,[3] and Ronen Zaidel-Bar[1,4,*]
[1]Department of Cell and Developmental Biology, Faculty of Medical & Health Sciences, Tel Aviv University, Tel Aviv 6997801, Israel
[2]Department of Molecular Life Sciences, University of Zurich, Winterthurerstrasse 190, CH-8057 Zurich, Switzerland
[3]Faculty of Biology, Technion - Israel Institute of Technology, Haifa 3200003, Israel
[4]Lead contact
*Correspondence: pritiag007@gmail.com (P.A.), zaidelbar@tauex.tau.ac.il (R.Z.-B.)
https://doi.org/10.1016/j.cub.2024.03.049

SUMMARY

Proper distribution of organelles can play an important role in a moving cell's performance. During *C. elegans* gonad morphogenesis, the nucleus of the leading distal tip cell (DTC) is always found at the front, yet the significance of this localization is unknown. Here, we identified the molecular mechanism that keeps the nucleus at the front, despite a frictional force that pushes it backward. The Klarsicht/ANC-1/Syne homology (KASH) domain protein UNC-83 links the nucleus to the motor protein kinesin-1 that moves along a polarized acentrosomal microtubule network. Interestingly, disrupting nuclear positioning on its own did not affect gonad morphogenesis. However, reducing actomyosin contractility on top of nuclear mispositioning led to a dramatic phenotype: DTC splitting and gonad bifurcation. Long-term live imaging of the double knockdown revealed that, while the gonad attempted to perform a planned U-turn, the DTC was stretched due to the lagging nucleus until it fragmented into a nucleated cell and an enucleated cytoplast, each leading an independent gonadal arm. Remarkably, the enucleated cytoplast had polarity and invaded, but it could only temporarily support germ cell proliferation. Based on a qualitative biophysical model, we conclude that the leader cell employs two complementary mechanical approaches to preserve its integrity and ensure proper organ morphogenesis while navigating through a complex 3D environment: active nuclear positioning by microtubule motors and actomyosin-driven cortical contractility.

INTRODUCTION

Organ morphogenesis involves cell and tissue movement through complex three-dimensional environments. As a result of their interactions with neighboring cells and the extracellular matrix (ECM), navigating cells experience multiple kinds of mechanical stress. How cells endure these physical challenges and maintain their shape and function, leading to robust organ formation, remains unclear.

An internal physical barrier to cell movement is the large and bulky nucleus.[1,2] Nevertheless, several studies revealed that actively positioning the nucleus at either the front or rear end of the cell facilitates migration in various ways. Rearward nuclear localization promotes polarization in fibroblast cells migrating on a 2D surface,[3] while in cells squeezing through a 3D matrix, it functions as a "piston": it is pulled forward by actomyosin contractility, pressurizing the cytoplasm and leading to forward movement.[4] Leukocytes employ their front-positioned nucleus as a "mechanical gauge" to identify the migratory path of least resistance[5] or to breach through the endothelial barriers.[6]

Nuclear positioning is mainly mediated by a well-conserved linker of the nucleoskeleton and cytoskeleton (LINC) complex.[7–10] It connects the nuclear envelope to the cytoskeletal networks of actin, microtubules, and intermediate filaments.[11,12] Mispositioning of the nucleus underlies multiple pathologies, such as embryonic lethality, lissencephaly, Emery-Dreifuss muscular dystrophy, and cardiomyopathy.[13,14] Despite the well-established role of nuclear positioning in several cellular contexts,[8,9] the significance of nuclear position and movement during organ morphogenesis remains largely unexplored.

Here, we investigated the role of nuclear localization during *C. elegans* gonad morphogenesis, wherein the nucleus of the somatic leader cell, known as the distal tip cell (DTC), is positioned at the front during the entire course of gonadogenesis.[15] The *C. elegans* gonad has two symmetrical U-shaped arms housing germ cells. Each of the gonadal arms is enwrapped within a basement membrane (BM) and sheath cells and is capped by a DTC. The DTC functions as a stem cell niche, promoting germ cell proliferation.[16,17] Previously, we revealed that the DTC is propelled by a pushing force exerted by the proliferating germ cells behind it.[18] The DTC secretes matrix-degrading metalloproteases and thus provides an outlet for the release of proliferative pressure, leading to directional gonad elongation. Furthermore, the DTC brings about gonad turning by asymmetrically positioning cell-matrix adhesions in response to chemotactic cues.[18–21]

Please cite this article in press as: Agarwal et al., Active nuclear positioning and actomyosin contractility maintain leader cell integrity during gonadogenesis, Current Biology (2024), https://doi.org/10.1016/j.cub.2024.03.049

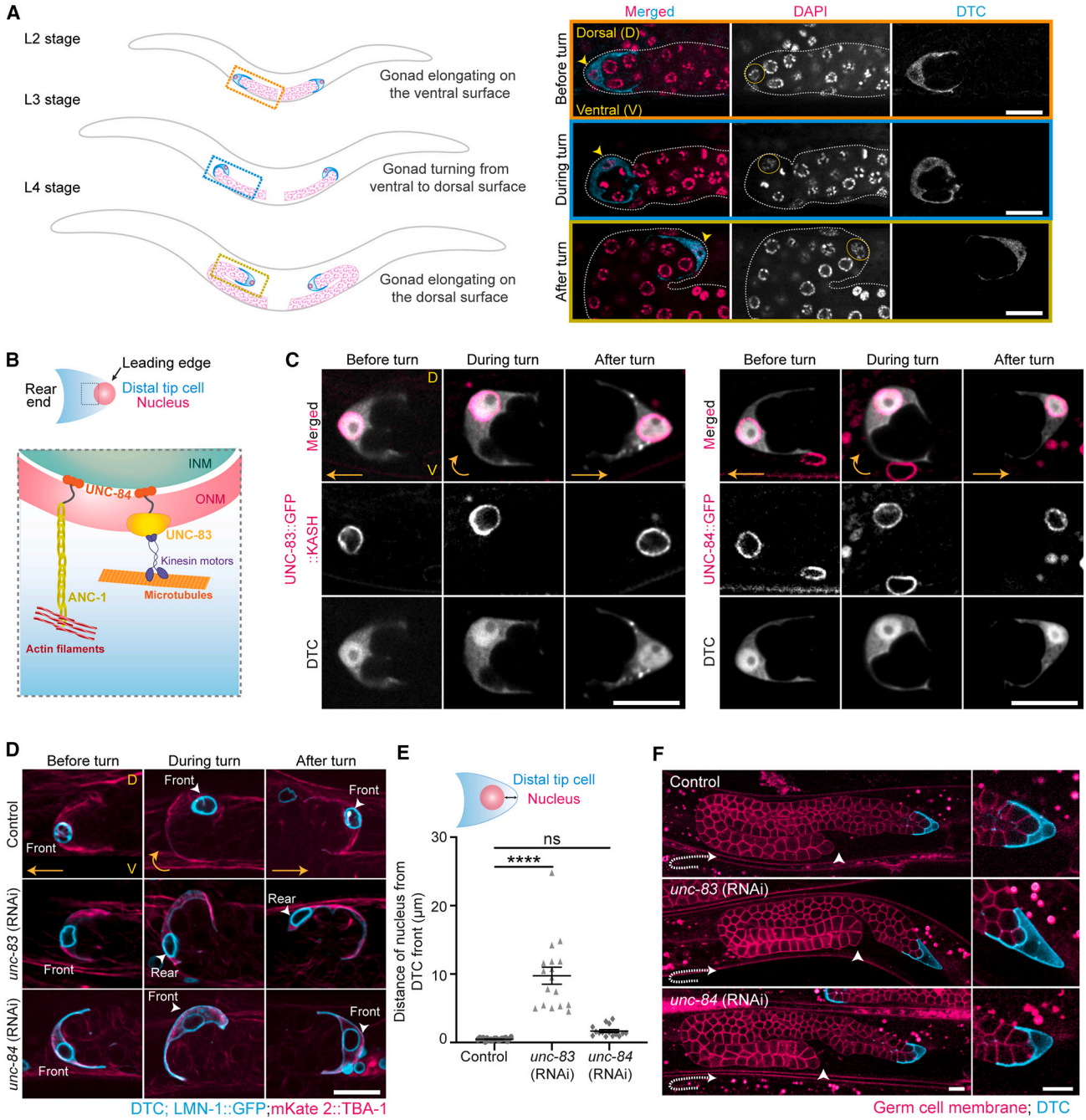

Figure 1. Nuclear positioning at the distal tip cell (DTC) front, mediated by UNC-83 and UNC-84, is dispensable for gonad morphogenesis

(A) Illustrations (left) and the respective microscopic images (right) of the 4',6-diamidino-2-phenylindole dihydrochloride (DAPI)-stained gonads expressing *lag-2p*::mNeonGreen (mNG)::PH show the position of the DTC nucleus before (orange box), during (blue box), and after the turn (green box). Pink, germ cell nuclei; blue, DTC; purple, DTC nucleus. Yellow arrowheads and circles indicate nucleus position within the DTC. White dotted lines outline the gonad.

(B) A schematic showing the localization of LINC complex proteins: the SUN protein, UNC-84 (orange), localizes at the inner nuclear membrane (INM), where it interacts with KASH proteins, UNC-83 (yellow) and ANC-1 (green), which reside on the outer nuclear membrane (ONM). On the cytoplasmic side, UNC-83 connects to microtubules, whereas ANC-1 is attached to actin filaments.

(C) Nuclear localization of UNC-83:GFP::KASH (left) and UNC-84::GFP (right) in a DTC expressing cytoplasmic *mig-24p*::WrmScarlet during different stages of gonad development.

(D) Representative images showing the position of the nucleus in DTCs expressing LMN-1::GFP, *lag-2p*::mNeonGreen:PH, and mKate2::TBA-1 in control versus DTC-specific *unc-83*(RNAi) and *unc-84*(RNAi) worms.

(legend continued on next page)

Please cite this article in press as: Agarwal et al., Active nuclear positioning and actomyosin contractility maintain leader cell integrity during gonadogenesis, Current Biology (2024), https://doi.org/10.1016/j.cub.2024.03.049

In this study, we found that the torque associated with gonad turning generates substantial stress on the DTC, which is alleviated by two cell-intrinsic mechanisms: frontal nuclear positioning and actomyosin contractility. Nuclear localization at the front of the DTC was dependent on the LINC complex protein UNC-83 and kinesin microtubule motor (kinesin light chain 2, KLC-2 and kinesin heavy chain, UNC-116). Nuclear mispositioning on its own did not affect gonad morphogenesis. However, DTC-specific depletion of non-muscle myosin II (NMY-2) contractility in conjunction with nuclear mispositioning led to an unexpected phenotype: DTC fragmentation and gonad bifurcation. Long-term live imaging revealed that, during the turn, the DTC fragmented into a nucleated cell and an enucleated cytoplast, each leading an independent gonadal arm. Strikingly, the enucleated cytoplast maintained polarity and secreted metalloproteases but could retain stem cell niche function only for a brief period. By integrating a mechanical model with quantitative imaging, we explain how nuclear position and cortical contractility regulate the force balance within the DTC, preserving its shape and integrity.

RESULTS

Nuclear positioning at the DTC front, mediated by LINC complex proteins UNC-83 and UNC-84, is dispensable for gonad morphogenesis

We examined nuclear position in the DTC of fixed worms stained with a chromatin marker (Figure 1A) as well as live worms expressing a cytoplasmic fluorescent marker (Figure S1A; Video S1). The leading edge or the front of the DTC is the side facing the direction of movement, while the rear end is closely adhered to germ cells (Figures 1A and 1B). We found the nucleus positioned at the extreme leading edge of the DTC—abutting the plasma membrane—as the gonad elongated on the ventral surface during the second larval stage (L2), consistent with previous reports.[15,22] During the third larval stage (L3), when the gonad made a U-turn, the DTC nucleus moved from the ventral toward the dorsal surface concomitantly with the movement of the cell body. After the turn, the gonad continued to elongate on the dorsal surface and the DTC nucleus retained its position at the leading edge (Figure 1A).

To investigate the mechanism regulating DTC nuclear positioning, we explored the role of three major LINC complex proteins: UNC-83, ANC-1, and UNC-84. UNC-83 and ANC-1 have conserved Klarsicht/ANC-1/Syne-1 homology (KASH) domains and localize on the outer nuclear envelope, while UNC-84, with a conserved Sad1/UNC-84 (SUN) domain, resides on the inner nuclear envelope[23–26] (Figure 1B). UNC-83, ANC-1, and UNC-84 are important for nuclear positioning in multiple tissues during *C. elegans* development.[23,24,27–31] ANC-1 is required for nuclear anchorage to actin filaments,[32,33] while UNC-83 interacts with microtubule motor proteins[34–36] (Figure 1B).

As shown in Figure 1C, both endogenously GFP-tagged UNC-83[37] and UNC-84[38] localized prominently around the DTC nucleus. Also, ANC-1 was present around the nucleus with more rearward enrichment (Figure S1B). Consistent with their localization, DTC-specific depletion of either UNC-83 or UNC-84 caused nuclear mispositioning within the DTC (Figures 1D and 1E). However, nuclear position was unaffected by DTC-specific depletion of ANC-1 (Figure S1B). Interestingly, the nucleus was not mispositioned while the gonad elongated on the ventral surface (Figure 1D, left) but began to deviate from its normal position at the front of the DTC, along the cell's symmetry axis, during the gonad turning phase (Figure 1D, middle). The nucleus remained mispositioned while the gonad elongated on the dorsal surface (Figure 1D, right). Thus, it appears that UNC-83 plays a critical role in nuclear movement during the gonadal turn. Notably, UNC-84 depletion caused the nucleus to be displaced slightly toward the rear, while retaining its position along the DTC axis of symmetry. In contrast, UNC-83 depletion resulted in a significant displacement of the nucleus from the front during the turn; the angular deviation of the nucleus increased with the progression of the DTC's turn, until it arrested at the rear edge of the DTC (Figures 1D and 1E).

Next, we investigated whether nuclear positioning at the leading edge of the DTC is essential for gonad morphogenesis. DTC-specific RNAi-mediated depletion of UNC-83, UNC-84, or ANC-1 did not affect DTC migration and gonad morphogenesis (Figures 1F, S1C, and S1D). We confirmed the efficiency of RNAi knockdown by carrying out *unc-83*(RNAi), *unc-84*(RNAi), and *anc-1*(RNAi) on endogenously GFP tagged proteins, and we observed 79%, 86%, and 91% reductions in their fluorescent intensity as compared to controls, respectively (Figures S1B and S1E–S1I). Together, these observations suggest that frontal DTC nuclear positioning is not essential for gonad morphogenesis, consistent with a previous report.[15]

Since gonad morphogenesis was unaffected by DTC nucleus mispositioning, we further explored if it impacts the fecundity of the worm or alters DTC architecture. DTC-specific depletion of UNC-83 did not affect germline function, as *unc-83*(RNAi) adult worms were able to form proper oocytes and embryos; however, the DTC structure was severely disrupted (Figure S1J).

Depletion of UNC-83 and non-muscle myosin II, NMY-2, results in DTC fragmentation and gonad bifurcation during the turn

Previously, we found that DTC-specific knockdown of several cytoskeletal proteins, including NMY-2, does not affect gonad morphogenesis.[18] This led us to hypothesize that some of these cytoskeletal elements function redundantly to regulate gonad morphogenesis. A candidate double-RNAi screen (Table S1) revealed that DTC-specific co-depletion of UNC-83 and NMY-2 resulted in multiple gonad morphogenesis defects, including turn defects (17%), failure to complete elongation (10%), and branched gonadal arms (42%) (no. of worms observed, $n = 59$) (Figures 2A and 2B).

(E) Quantification of nuclear displacement from the DTC front (as shown in schematic) in control ($n = 19$) versus DTC-specific *unc-83*(RNAi) ($n = 17$) and *unc-84*(RNAi) ($n = 15$) worms. Statistical analysis was carried out using one-way ANOVA. **** indicates p value < 0.0001; ns, not significant.

(F) Representative images showing the morphology of gonads expressing a germ cell membrane marker (pie-1:mCherry:PH, pink) and a DTC membrane marker (*lag-2p*::mNeonGreen:PH, cyan) in control ($n = 37$) versus DTC-specific *unc-83*(RNAi) ($n = 35$) and *unc-84*(RNAi) ($n = 29$) worms. Insets on the right display magnified images of the DTC. Orange arrows indicate the direction of DTC movement. Scale bar, 10 μm. See also Figure S1 and Video S1.

Please cite this article in press as: Agarwal et al., Active nuclear positioning and actomyosin contractility maintain leader cell integrity during gonadogenesis, Current Biology (2024), https://doi.org/10.1016/j.cub.2024.03.049

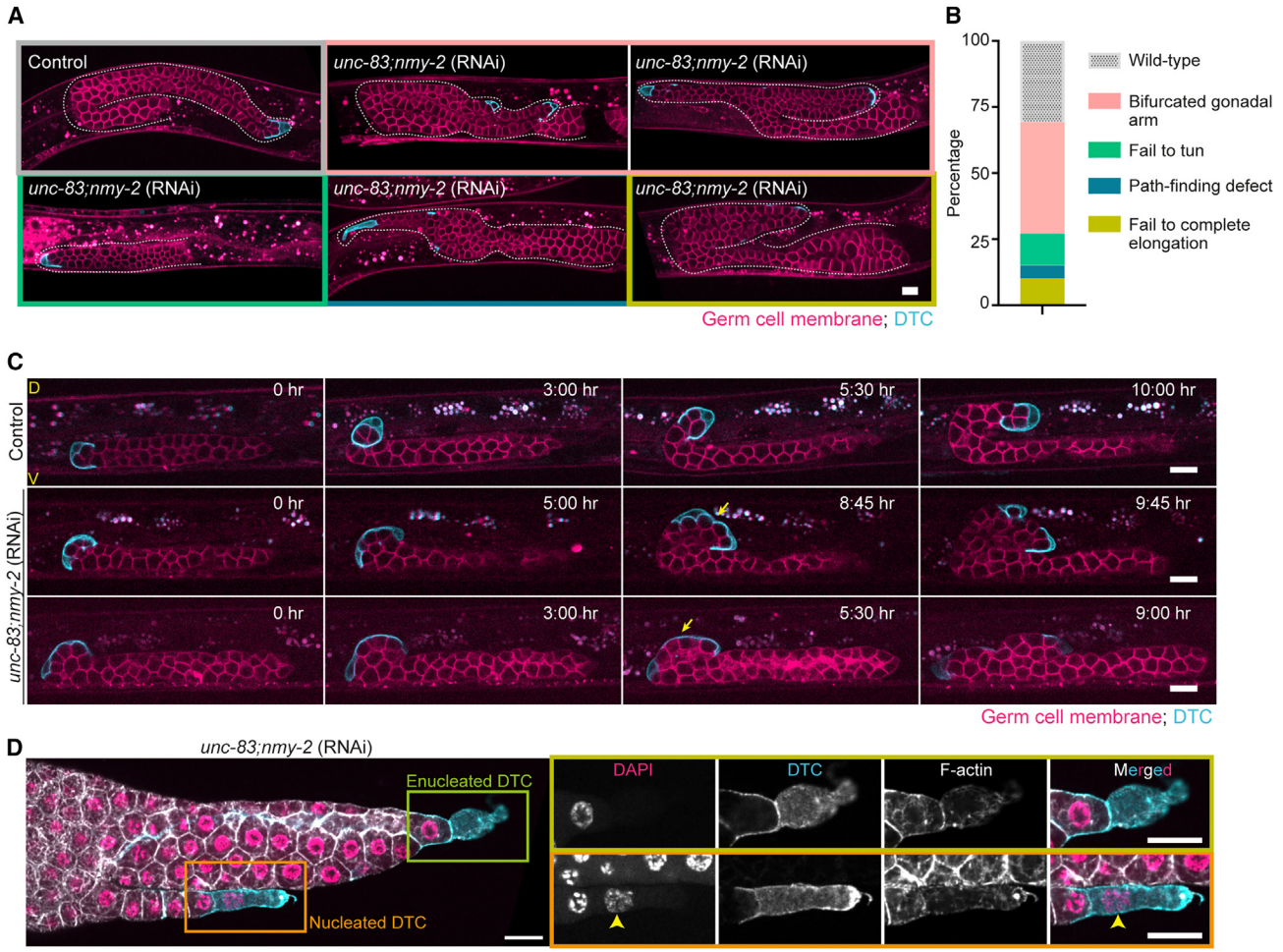

Figure 2. Formation of an enucleated DTC and a bifurcated gonadal arm after DTC-specific depletion of UNC-83 and NMY-2

(A) Representative images showing the morphology of gonads expressing a germ cell membrane marker (pie-1:mCherry:PH, pink) and a DTC membrane marker (*lag-2p*:mNeonGreen:PH, cyan) in control (n = 44) versus DTC-specific *unc-83; nmy-2* (RNAi) (n = 59) worms.

(B) Percentage of gonad morphology defects observed in DTC-specific depleted *unc-83;nmy-2*(RNAi) worms. Color code corresponds to the defects shown in (A).

(C) Images from time-lapse videos of gonads expressing a germ cell membrane marker (pie-1:mCherry:PH, pink) and a DTC membrane marker (*lag-2p*:mNeonGreen:PH, cyan) in control (top) and DTC-specific *unc-83;nmy-2*(RNAi) worms (middle and bottom). The middle panel depicts an example in which DTC fragments move in the same direction after the turn, while the bottom panel shows an example where, after DTC fragmentation, gonadal arms elongate in opposite directions. Yellow arrows indicate the site of DTC splitting.

(D) Representative image of the bifurcated gonadal arms of DTC-specific *unc-83;nmy-2*(RNAi) worms expressing a DTC membrane marker (*lag-2p*:mNeonGreen:PH, cyan) and stained with an F-actin marker (phalloidin, gray) and a nuclei marker (DAPI, pink). Magnified insets on the right show an enucleated DTC (top, green box) and nucleated DTC (bottom, orange box). Yellow arrowheads point to the DTC nucleus. Scale bar, 10 μm. See also Figures S1–S4, Table S1, and Video S2.

Surprisingly, DTC-specific co-depletion of UNC-84 and NMY-2 resulted in a much milder phenotype, with only 7% of the worms having branched gonadal arms (Figures S1D and S1K). We did not see any gonad morphogenesis defects after DTC-specific co-depletion of ANC-1 and NMY-2 (Figures S1C and S1D). We tested the efficacy of UNC-84 and ANC-1 knockdown and found the intensity of endogenous UNC-84::GFP was reduced to 18% in *unc-84;nmy-2*(RNAi) worms, while endogenous ANC-1::GFP intensity decreased to 9% in *anc-1;nmy-2*(RNAi) worms as compared to control (Figures S1B–S1E, S1H, and S1I). Together, these results indicate that UNC-83 and NMY-2 function redundantly to ensure proper gonad morphogenesis. UNC-83 is known to transmit force from the cytoplasm to the nucleus by interacting physically with the inner nuclear envelope SUN domain protein UNC-84 during embryogenesis.[39,40] The milder phenotype observed in *unc-84;nmy-2*(RNAi) worms as compared to *unc-83;nmy-2*(RNAi) worms indicates either that UNC-83 interacts with a different SUN protein present in the inner nuclear envelope of the DTC or that the observed phenotype results from non-LINC-complex-dependent function of UNC-83, as reported for ANC-1.[30]

To better understand the functional redundancy between UNC-83 and NMY-2, we studied the localization of NMY-2 and its role in nuclear positioning within the DTC. Endogenously tagged NMY-2 showed significant enrichment at the rear end of the DTC during different stages of gonad development (Figure S2A). Depletion of NMY-2 did not affect nuclear position within the DTC; however, unlike in control worms, we observed

Please cite this article in press as: Agarwal et al., Active nuclear positioning and actomyosin contractility maintain leader cell integrity during gonadogenesis, Current Biology (2024), https://doi.org/10.1016/j.cub.2024.03.049

the presence of long DTC membrane extensions (Figure S2B). We confirmed efficient depletion of NMY-2 (>95%) by measuring the fluorescence intensity of endogenously tagged NMY-2::mKate after *nmy-2*(RNAi) and *unc-83;nmy-2*(RNAi) (Figures S2B and S2C).

Since the majority of *unc-83;nmy-2*(RNAi) worms had branched gonadal arms, we focused our attention on this novel phenotype. To trace the origin of the branched gonad phenotype, we employed a microscope-mounted microfluidic device that permits long-term imaging.[41] As shown in Video S2 and Figure 2C (upper), imaging of worms with fluorescently labeled DTC and germ cell membranes, from the L3 stage until the late L4 stage, allowed us to capture the dynamics of gonad ventral elongation, turning, and dorsal elongation. Importantly, imaging of DTC-specific *unc-83;nmy-2*(RNAi) worms revealed that during the turn, the DTC breaks apart into two cell fragments (Figure 2C; Video S2). After the turn, we observed two different outcomes of the DTC breaking apart into a nucleated cell and an enucleated cytoplast. In most (67%) cases, both the cell- and cytoplast-led gonadal arms elongated in the same direction, toward the midbody of the worm (Figure 2C, middle; Video S2). In a third of the cases, the cell- and cytoplast-led gonad arms elongated in opposite directions (Figure 2C, bottom; Video S2). Either way, the enucleated fragment formed from the front of the cell while the nucleated fragment formed from the rear of the DTC. Remarkably, the gonadal arm elongating on the dorsal surface in the wrong direction—i.e., away from the midbody—invariably was led by the nucleated DTC, while the enucleated DTC led the gonad arm elongating in the correct direction. Also, in the majority (75%) of cases, the gonadal arm led by the enucleated DTC elongated further than the gonadal arm led by the nucleated DTC.

To confirm that the DTC is torn apart during the turn and does not undergo normal cell replication and division, we stained gonads expressing a DTC membrane marker with a nuclear marker and an F-actin marker. As evident in Figure 2D, after DTC-specific co-depletion of UNC-83 and NMY-2, one cell fragment contained the nucleus while the other one was enucleate. This phenotype of DTC fragmentation is distinct from the phenotype of extra DTCs[42] formed due to transdifferentiation of somatic cells into DTCs,[43] hyperproliferation of DTCs,[44] and abnormal cell-fate specification[45] in that additional DTCs in these cases have nuclei. For example, each of the ectopic DTCs formed at the expense of an anchor cell, following the depletion of the nuclear hormone receptor NHR-25,[46] have a nucleus (Figure S3).

DTC fragmentation is not due to an inability to detach cell-matrix adhesions

Cellular fragmentation is a known phenotype in cultured motile cells with impaired myosin contractility.[47,48] Previous studies have demonstrated this effect in cells that utilize crawling motility, in which the adhesions at the rear of the cell generate resistive forces that pull the cell backward, while actin polymerization at the front pushes it forward.[49] Myosin contractility pulls against the resisting rear adhesions, thereby lowering the elastic stress in the cell. Without myosin contractility, these opposing forces produce a large stress in the elastic cellular elements (such as the plasma membrane and passive cytoskeleton), leading to fragmentation. In contrast to these findings, our previous study showed that the propulsive force for DTC motility is provided by external pressure exerted on the DTC by the bulk of the gonad.[18] Cell-substrate adhesions are not required for forward motion in this case but are rather utilized for steering.[18] Consistently, DTC-specific depletion of NMY-2 did not cause DTC fragmentation, although we observed the presence of long DTC membrane extensions (Figures S2B and S4A). We propose that these long extensions are attributable to reduced cortical contractility rather than due to the inability of the DTC to detach itself from the substrate in the absence of NMY-2. Consistent with this hypothesis, attenuation of cell-matrix adhesions by depleting α-integrin INA-1 along with NMY-2 failed to prevent the formation of membrane extensions (Figure S4A). The presence of gonadal arms displaying turn defects indicated efficient depletion of INA-1 in *ina-1;nmy-2*(RNAi) worms. We also quantified INA-1 knockdown percentage by carrying out *ina-1;nmy-2*(RNAi) on the worms expressing INA-1::mNG. We observed a 93% reduction in INA-1::mNG intensity as compared to control (Figures S4B and S4C). Together, these results show that long DTC membrane extensions formed in the absence of NMY-2 are not due to strong DTC-matrix adhesions, and therefore DTC fragmentation is not likely a result of its inability to detach cell-matrix adhesions.

Enucleated DTCs can invade but do not retain stem cell niche function for long

Cell shape and polarity, which are important for cell invasion and vesicular trafficking, are maintained by cell adhesion and the cytoskeleton. Intrigued by the observation that the enucleate DTC supports gonad elongation, we investigated its cytoskeletal organization in comparison with nucleated DTCs. No notable difference was observed in the localization pattern of F-actin (Figure 2D), β-integrin/PAT-3 (Figure 3A), Talin/TLN-1, or the actin nucleator Arp2/ARX-2 (Figure 3B) between the nucleated DTC fragment and the enucleated DTC cytoplast. Consistent with their ability to lead gonad arm elongation, we found that enucleated DTCs also exhibited polarized localization of the metalloprotease GON-1[18,50,51] (Figure 3C). Also, both gonadal arms, led by nucleated and enucleated DTC, were surrounded by laminin, a BM component (Figure 3D). Altogether, these results indicate that after DTC fragmentation, the enucleated DTC cytoplast recapitulates the structure of a nucleated DTC.

To test whether the enucleated DTC is under pressure from the germ cells, as was shown for the normal DTC,[18] we performed laser incision experiments on the BM. A small incision at a region behind the enucleated DTC caused an instant release of pressure, indicating the presence of proliferative pressure within the gonadal arm led by enucleated DTC (Video S3). This is consistent with our previous study, where we showed the presence of proliferative pressure not only behind the DTC but also far from the DTC in the loop region.[18]

Since the DTC also functions as a stem cell niche, promoting the proliferation of adjacent germ cells through GLP-1/Notch signaling,[16,52] we examined whether the DTC cytoplast can support germline stemness. To this end, we examined larval and adult gonads for expression of SYGL-1, a downstream target of GLP-1/Notch signaling.[17,53–55] Interestingly, gonadal arms led by enucleated DTC cytoplasts showed a progressive decline in the level of SYGL-1 with increasing age, and no staining was

Please cite this article in press as: Agarwal et al., Active nuclear positioning and actomyosin contractility maintain leader cell integrity during gonadogenesis, Current Biology (2024), https://doi.org/10.1016/j.cub.2024.03.049

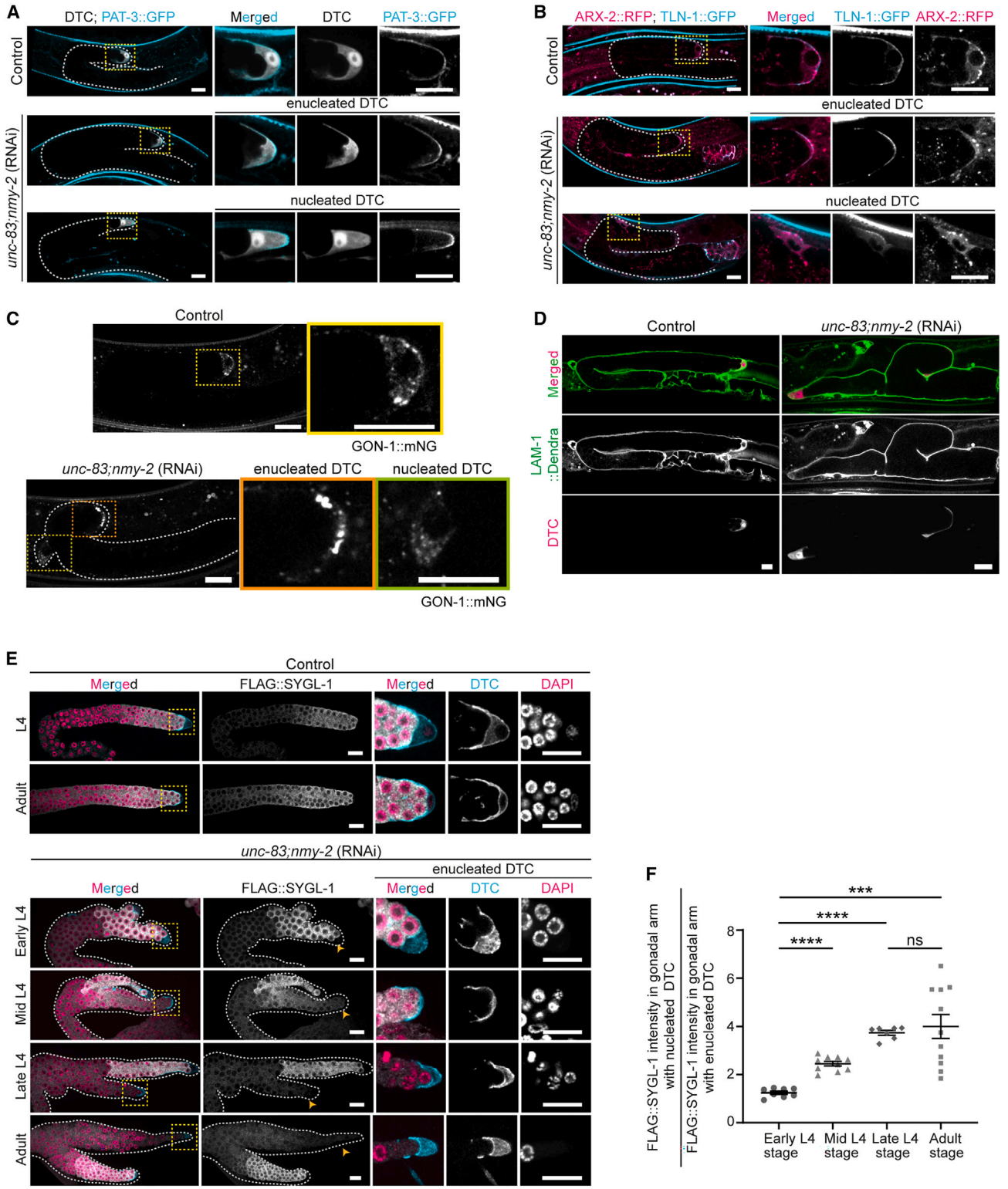

Figure 3. Enucleated DTC can invade but loses stem cell niche function over time

(A) Representative images of a gonad expressing GFP::PAT-3 (cyan) and a DTC marker (*mig-24p*::WrmScarlet, gray) in control and *unc-83;nmy-2*(RNAi) worms. Magnified views of the DTCs are shown on the right, depicting enucleated and nucleated DTCs from different Z-planes of the same gonad.

(legend continued on next page)

detected in the adult stage. In contrast, SYGL-1 staining was retained in the gonadal arm with a nucleated DTC in the larval and adult stages as seen in the control (Figures 3E and 3F). Consistently, in the adults with bifurcated gonad arms, dividing germ cells, identified by their mitotic spindle, were observed only in the gonadal arm with the nucleated DTC (Figure S5). These results indicate that enucleated DTCs can initially function as stem cell niches but progressively lose this ability. Collectively, these results indicate that enucleated DTC retains its architecture and invasive activity but fails to sustain the stem cell niche function for an extended period.

A polarized acentrosomal microtubule network and kinesin-1 activity are responsible for the frontal nuclear position required to preserve DTC integrity during the turn

Given that UNC-83 is linked to the microtubule network, we next explored whether DTC fragmentation in the absence of UNC-83 and NMY-2 is related to a cell-wide disruption of the DTC's microtubule cytoskeleton. Examining endogenously tagged α-tubulin/TBA-1, we did not discern any defects in the organization of microtubules after DTC-specific depletion of UNC-83 alone or together with NMY-2 (Figure 4A). We further analyzed microtubule polarity and dynamics in the DTC using an endogenously mKate2-tagged microtubule end binding protein, EBP-2,[56] which labels the plus-end tips of growing microtubules.[57] We observed that most microtubules grow from the rear end toward the leading edge of the DTC in control worms, and this directionality was unaffected in *unc-83*(RNAi) and *unc-83;nmy-2*(RNAi) worms (Figure 4B; Videos S4 and S5). Given this polarity, we visualized centrosomes in the gonad with endogenously tagged TAC-1 and ZYG-9[58] and found that the DTC microtubule network is acentrosomal (Figure S6A). This was further confirmed by temporal projection views of the time-lapse videos of EBP-2::mKate2. The EBP-2 comet tracks did not grow from any single point, consistent with acentrosomal microtubules (Figure S6B). To assess microtubule dynamics, we measured the growth length and speed of EBP-2 comets. Growth length and speed were unaffected in the nucleated DTC of *unc-83*(RNAi) (growth length = 1.1 ± 0.03 μm; speed = 0.73 ± 0.05 μm/s, $n = 10$) and *unc-83;nmy-2*(RNAi) worms (growth length = 1.17 ± 0.05 μm; speed = 0.66 ± 0.03 μm/s, $n = 11$) but were moderately increased in enucleated DTC of *unc-83;nmy-2*(RNAi) worms (growth length = 1.27 ± 0.07 μm; speed = 0.75 ± 0.02 μm/s, $n = 9$) as compared to the control (growth length = 1 ± 0.03 μm; speed = 0.60 ± 0.02 μm/s, $n = 11$) (Figure 4C). Thus, depletion of UNC-83 does not perturb microtubule organization and dynamics. No significant difference in the microtubule organization was observed between the nucleated and enucleated DTC of *unc-83;nmy-2*(RNAi) worms, but they grow slightly longer and faster without a nucleus.

UNC-83 functions as a cargo adapter, connecting the nucleus with three microtubule motor protein complexes[31,36]: a kinesin-1 complex[34] (KLC-2/UNC-116) and two dynein complexes (BICD-1/EGAL-1/DLC-1 and NUD-2/LIS-1).[35,59] Therefore, we investigated which motor proteins are responsible for maintaining the nucleus at the front of the DTC and whether this is how UNC-83 prevents cell fragmentation in the absence of NMY-2. We performed DTC-specific RNAi against proteins from each of the three complexes. DTC depletion of LIS-1 and DLC-1 showed a slight displacement of the nucleus from the leading edge, while the nucleus was substantially displaced toward the rear end of the DTC after the depletion of KLC-2 or UNC-116 (Figures 5A and 5B), phenocopying the knockdown of UNC-83 (Figures 2A–2C). These results demonstrate that the major force for DTC movement and positioning at the cell front is provided by the plus-end-directed motor protein kinesin-1. This conclusion is congruous with our EBP2::mKate2 data, which showed plus-end growth directed toward the leading edge of the DTC (Figure 4B; Video S4). In accordance with their minor role in DTC nuclear positioning, DTC-specific knockdown of dynein motor proteins, on its own or in combination with NMY-2 depletion, did not show any defect in gonad morphogenesis. In contrast, DTC-specific *klc-2*(RNAi) and *unc-116* (RNAi) worms showed the splitting of gonadal arms phenotype with low penetrance (3.4%; $n = 60$ and 5.6%; $n = 53$, respectively), and this defect was considerably enhanced when the kinesin motor was depleted along with NMY-2 (15%; $n = 53$ and 23%; $n = 53$, respectively). In addition, such cells showed path-finding defects, failure to turn, and failure to complete elongation phenotypes (Figures 5C and 5D). These results suggest that active forces mediated via UNC-83 and kinesin-1 motor activity are responsible for maintaining the nucleus at the front of the DTC and that this frontal position is essential to preserve the integrity of the cell during the turn, especially in the absence of NMY-2. Furthermore, the kinesin results rule out the possibility that gonad bifurcation is the result of changes in gene expression due to the absence of UNC-83.

A mechanical model explains how nuclear positioning and contractility safeguard DTC integrity during the gonadal turn

To gain further insight into the cause of DTC fragmentation, we closely examined the morphology of the DTC during the turn in control, *nmy-2*(RNAi), *unc-83*(RNAi), and *unc-83;nmy-2*(RNAi)

(B) Representative images of a gonad expressing ARX-2::RFP (pink) and GFP::TLN-1 (cyan) in control and *unc-83;nmy-2* (RNAi) worms. Enlarged views of the DTCs are shown on the right, depicting enucleated and nucleated DTCs from different Z-planes of the same gonad.
(C) Representative images of a gonad expressing GON-1::mNeonGreen (mNG) in control and *unc-83;nmy-2*(RNAi) worms. Magnified insets show the localization of GON-1::mNG in the DTCs in different conditions.
(D) Representative images of a gonad expressing LAM-1::Dendra (green) and a DTC marker (*mig-24p*::WrmScarlet, pink) in control and *unc-83;nmy-2*(RNAi) worms.
(E) Representative images of anti-FLAG antibody (gray) and DAPI (a nuclear marker, pink) stained gonads in control and DTC-specific depleted UNC-83 and NMY-2 worms. These gonads express FLAG::SYGL-1, a mitotic germ cell marker, and a DTC membrane marker (*lag-2p*::mNeonGreen::PH, cyan). An orange arrowhead highlights the gonadal arm led by an enucleated DTC.
(F) Quantification of FLAG::SYGL-1 intensity in the branched gonads of *unc-83;nmy-2*(RNAi) worms with nucleated versus enucleated DTC (early L4 stage, $n = 8$; mid-L4 stage, $n = 10$; late L4 stage, $n = 7$; adult stage, $n = 11$). Statistical analysis was carried out using one-way ANOVA. **** indicates p value < 0.0001; *** indicates p value < 0.001; ns, not significant. Scale bar, 10 μm. See also Figure S5 and Video S3.

Please cite this article in press as: Agarwal et al., Active nuclear positioning and actomyosin contractility maintain leader cell integrity during gonadogenesis, Current Biology (2024), https://doi.org/10.1016/j.cub.2024.03.049

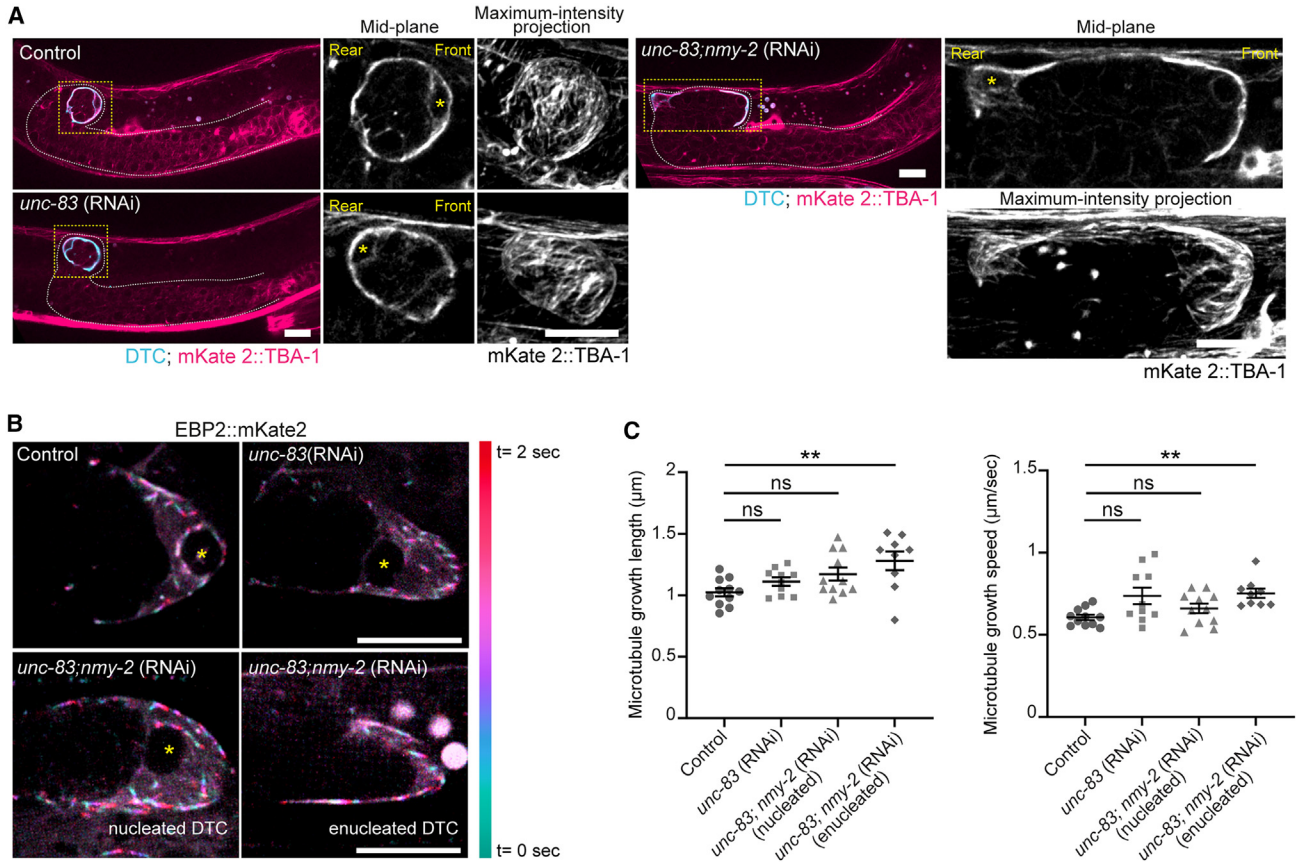

Figure 4. A polarized microtubule network in the DTC is unaffected by *unc-83* RNAi, and enucleated DTC cytoplasts have moderately enhanced microtubule dynamics

(A) Representative images of gonads expressing mKate2::*TBA-1* (pink) and a DTC marker (*mig-24p*::WrmScarlet, cyan) in control versus DTC-specific depleted *unc-83*(RNAi) *and unc-83;nmy-2*(RNAi) worms. Magnified insets on the right display mid-plane and maximum-intensity projected views of the DTCs. Yellow asterisks indicate the position of the DTC nucleus.

(B) Representative time-lapse color-coded images of EBP-2::mKate2 in the DTC of control versus *unc-83*(RNAi) *and unc-83;nmy-2*(RNAi) worms to show microtubule growth directionality. Images were acquired at 200 ms intervals for a period of 2 s. Green color denotes the first time point, while red denotes the end time point. Yellow asterisks indicate the position of the DTC nucleus.

(C) Microtubule growth length and growth rate in the DTC of control versus *unc-83*(RNAi) *and unc-83;nmy-2*(RNAi) worms. Statistical analysis was carried out using one-way ANOVA. ** indicates p value < 0.01; ns, not significant. Scale bar, 10 μm. See also Figure S6 and Videos S4 and S5.

worms. Depletion of NMY-2 or UNC-83 on their own did not have an obvious effect on DTC morphology. However, their concurrent depletion led to a significant deformation of the DTC (Figure 6A). We quantified the perimeter and aspect ratio of the entire DTC and the average radius of curvature along the DTC front edge for the various conditions. We found that knockdown of NMY-2 showed a mild defect, but when combined with the knockdown of UNC-83 the DTC adopts a more elongated shape with a significantly higher radius of curvature than the control (Figure 6B).

To explain these observations, we propose an expanded mechanical model for the role of the DTC nucleus in maintaining cellular integrity throughout the gonad morphogenesis process. According to our model, pressure from proliferating cells in the bulk of the gonad is the driving force behind DTC motion. The mechanical role of the DTC during elongation is to cap the elongating end of the gonad and to steer its path.[18] During gonad turning, the DTC develops an asymmetric adhesion pattern, with a highly adherent region in its dorsal region. The pressure from the bulk of the gonad applies a bending moment to the DTC about the adherent region, resulting in DTC rotation.[18] Throughout the DTC's progress, its nucleus experiences increased friction with the surrounding environment due to its size and rigidity, and, subsequently, is under greater resistance to motion than the rest of the cell. This assumption is supported by the observation that the gonadal arm led by the enucleated DTC elongated faster than the arm led by the nucleated DTC in the majority of *unc-83;nmy-2*(RNAi) worms. As the pressure in the gonad is expected to equilibrate rapidly in comparison with its rate of motion,[60] an equal pushing force is applied to both the enucleated and nucleated branches. The reduced speed of the nucleated branch is therefore explained by the nucleus' traction. This finding is in agreement with previous studies showing that the nucleus produces additional resistance to motion in a confined environment.[61,62]

Since the DTC's nucleus experiences increased traction, kinesin-based active forces are required to counter this friction and

Please cite this article in press as: Agarwal et al., Active nuclear positioning and actomyosin contractility maintain leader cell integrity during gonadogenesis, Current Biology (2024), https://doi.org/10.1016/j.cub.2024.03.049

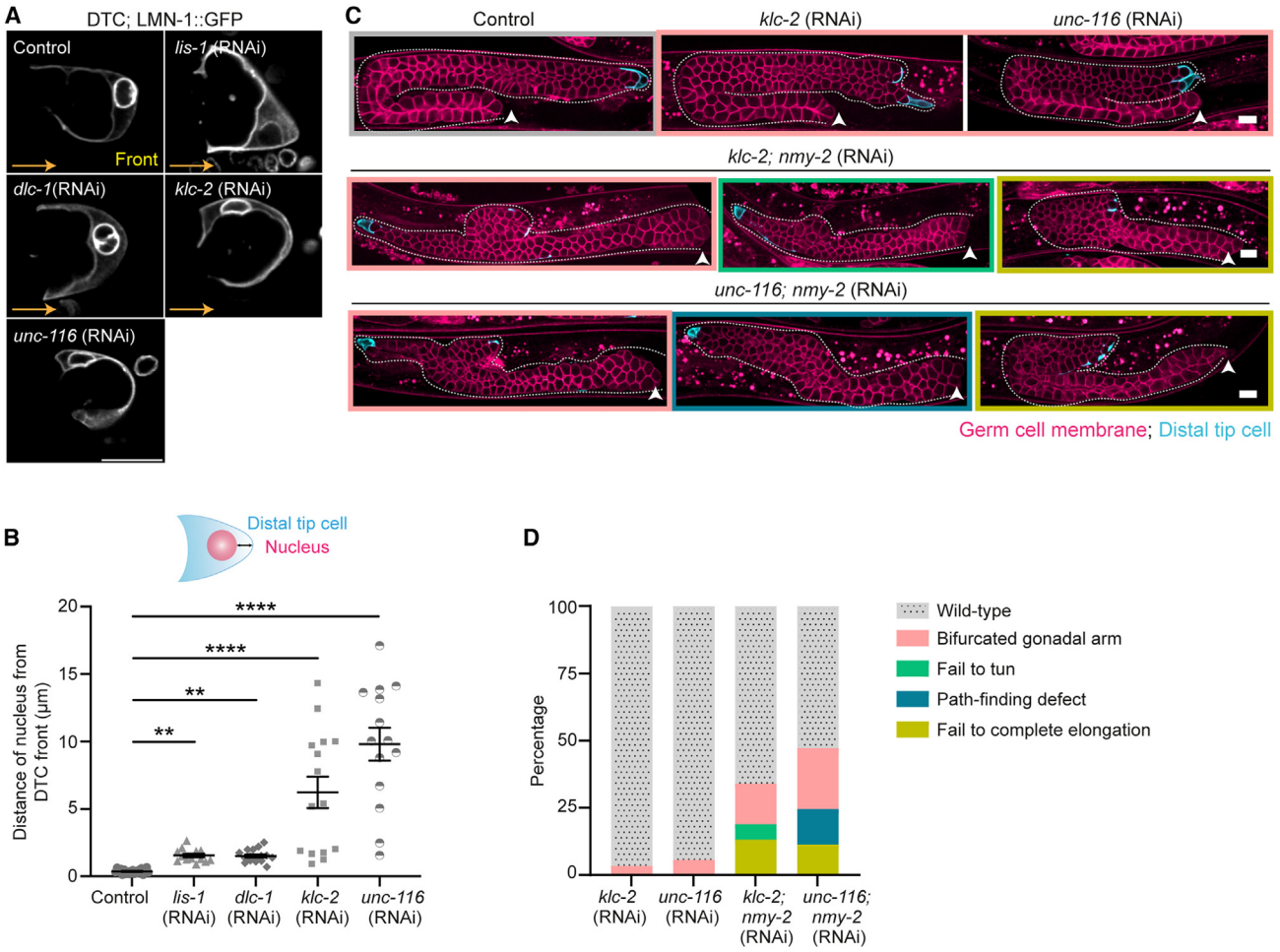

Figure 5. Active nuclear positioning by kinesin-1 and non-muscle myosin II contractility together preserve DTC integrity during gonad morphogenesis

(A) Representative images showing the position of the nucleus in a DTC expressing LMN-1-*1*::GFP; *lag-2p*::mNeonGreen:PH in control worms and after DTC-specific depletion of the dynein regulator LIS-1, dynein light chain 1 (DLC-1), kinesin light chain 2 (KLC-2), and kinesin heavy chain (UNC-116).

(B) Quantification of nuclear displacement from the DTC front in control (n = 20) versus DTC-specific RNAi depletion of *lis-1* (n = 13), *dlc-1* (n = 16), *klc-2* (n = 15), and *unc-116* (n = 14) worms. Statistical analysis was carried out using one-way ANOVA. **** indicates p value < 0.0001; ** indicates p value < 0.01.

(C) Representative images showing gonad morphology in worms expressing a germ cell membrane marker (*pie-1*::mCherry:PH, pink) and a DTC membrane marker (*lag-2p*::mNeonGreen:PH, cyan) in control versus DTC-specific RNAi depletion of *klc-2*, *unc-116*, *klc-2;nmy-2*, and *unc-116;nmy-2*.

(D) Percentage of different gonad morphology defects observed in DTC-specific *klc-2*(RNAi) (n = 60), *unc-116*(RNAi) (n = 67), *klc-2;nmy-2*(RNAi) (n = 53), *unc-116;nmy-2*(RNAi) (n = 53). Color code corresponds to the gonad morphology defects shown in (C). Orange arrows indicate the direction of DTC movement. Scale bar, 10 µm.

rotate the nucleus together with the rest of the cell about the high-adhesion pivot region (Figure 6C, control). Disruption of the microtubule positioning mechanism results in lagging of the nucleus behind the overall rotation of the DTC (Figure 6C, *unc-83*). Whereas the entire DTC is under proliferating pressure from the gonad bulk, friction with the environment is relatively localized to the nucleus and to the adhesion sites at the dorsal surface of the DTC. When the nucleus is actively positioned near this adhesion site, the DTC can rotate about this common anchoring region, leading to gonad bending. However, when the nucleus becomes mispositioned to the cell region furthest from the adhesion site, the DTC cap is essentially anchored by both the nucleus and the adherent region. Under such conditions the gonad pressure, P, will act to expand, rather than rotate the DTC cap, resulting in stretching tension, τ_{tot} within it (Figure 6C, *unc-83* and *unc-83;nmy-2*).

While a direct measurement of the mechanical stress in the DTC is not available, this value may be qualitatively estimated by neglecting the cell thickness and coarsely considering the DTC as a curved cap. The total DTC tension, τ_{tot}, that is required to resist the pressure is given by the Laplace relation $\tau_{tot} \sim R_c \cdot P$, where R_c is the radius of curvature of the DTC cap. External stretching forces applied to cells are countered by two types of intracellular stress: active actomyosin contractility as well as passive stress due to the resistance to deformation of elastic cellular elements, such as the cell membrane,[63,64] so that the total tension in the DTC cap is $\tau_{tot} = \tau_{act} + \tau_{el}$. The passive stress falling on the elastic elements of the DTC is

Please cite this article in press as: Agarwal et al., Active nuclear positioning and actomyosin contractility maintain leader cell integrity during gonadogenesis, Current Biology (2024), https://doi.org/10.1016/j.cub.2024.03.049

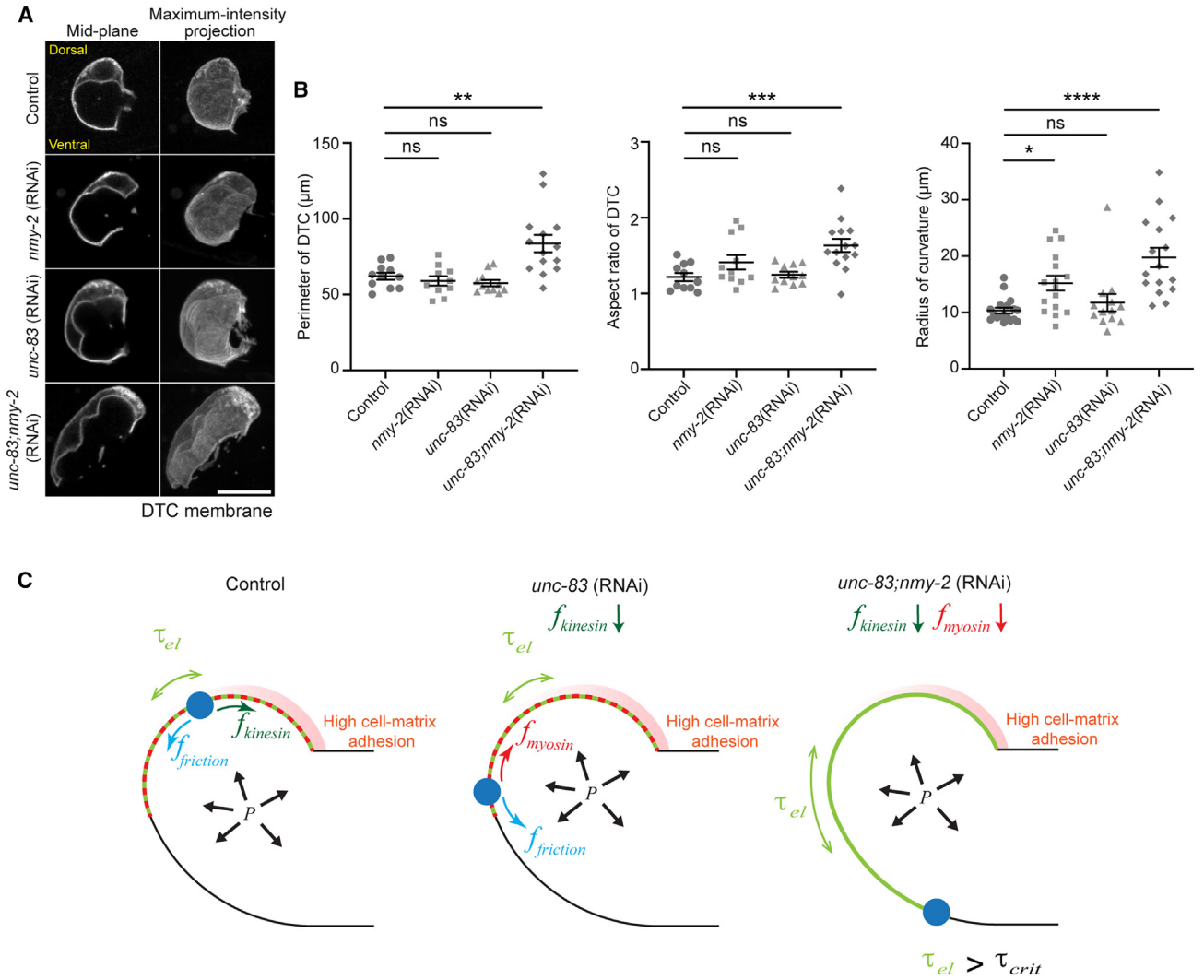

Figure 6. Excessive mechanical strain, due to nuclear mispositioning and reduced actomyosin contractility, leads to DTC fragmentation

(A) Midplane and maximum-intensity projection views of DTCs expressing *lag-2p*:mNG::PH in control versus DTC-specific *unc-83*(RNAi), *nmy-2*(RNAi), and *unc-83;nmy-2*(RNAi) worms during the turn from the ventral to dorsal surface. Scale bar, 10 µm.

(B) Quantification of perimeter, aspect ratio, and cell-averaged radius of curvature of maximum-intensity projection views of DTCs (as shown in A) in control (n = 11, 11 and 18) versus DTC-specific *unc-83*(RNAi) (n = 11, 11 and 13), *nmy-2* (RNAi) (n = 10, 11 and 16), and *unc-83;nmy-2*(RNAi) (n = 14, 14 and 16) worms. **** indicates p value < 0.0001; *** indicates p value < 0.001; ** indicates p value < 0.01; * indicates p value < 0.05.

(C) Schematic representation of DTC forces. During the turn, the DTC nucleus (blue circle) is localized at the front, close to the region of high adhesion (pink), in a balance between a frictional force exerted on the nucleus $f_{friction}$ and a kinesin based restoring force $f_{kinesin}$. The DTC has both elastic τ_{el} and active contractile elements f_{myosin} (red-green dashed curve) that resist the pressure from the gonad (P) (control). Depletion of the kinesin-based restoring force $f_{kinesin}$ (*unc-83* (RNAi)) mislocalizes the nucleus away from the site of high adhesion. DTC shape is maintained by a force balance between friction force exerted on the nucleus $f_{friction}$ and actomyosin force f_{myosin} against the gonadal pressure (P). A DTC with impaired $f_{kinesin}$ and f_{myosin} (*unc-83;nmy-2*(RNAi)) stretches and elongates (between two anchor points, i.e., the mislocalized nucleus and region of high adhesion) due to increased elastic tension τ_{el} (green curve). Beyond a critical threshold τ_{crit}, increased elastic tension τ_{el} leads to DTC fragmentation.

therefore given by $\tau_{el} = R_c \cdot P - \tau_{act}$ and is elevated both by increase in R_c as well as by decrease in τ_{act}. A rise of the elastic stress beyond some critical threshold $\tau_{el} > \tau_{crit}$ will lead to DTC fragmentation[65,66] (Figure 6C, *unc-83;nmy-2*). We note that the radius of curvature of the DTC edge is not constant, indicating variations in the localized traction forces with the environment. We therefore utilize an averaged value of the curvature along the edge, thereby partially obscuring the observed flattening effect. We further note that in cases where the DTC is spread over the gonad's bent region (Figure 2C), the inherent bending rigidity of the gonad's bulk strongly affects the curvature of the outer edge,[18] further reducing the accuracy of this estimate of the internal DTC tension.

Based on this qualitative model, we understand that the function of the active positioning by kinesin motors is to keep the nucleus close to the cell adhesions in order to allow the DTC to rotate about a common region of high friction while maintaining the cell shape. It is further seen that myosin activity may play a

double role in preventing DTC fragmentation: myosin contractility both limits the deformation of the DTC, preventing an increase in the total stress, and relieves some of the stress that falls on the passive elastic elements in the cell. Failure of both the kinesin- and myosin-based forces results in acute cell deformation, mechanical strain, and subsequent fragmentation of the DTC.

DISCUSSION

The DTC employs two complementary mechanical mechanisms, active nuclear positioning by microtubule motors and actomyosin-driven cortical contractility, in order to preserve its integrity and ensure proper organ morphogenesis while navigating through a complex 3D environment. A similar approach might be employed during morphogenesis of branched organs, such as lungs, kidneys, and salivary glands. Relying on more than one mechanism to maintain leader cell integrity confers robustness to the process of organogenesis. Multiple mechanical processes acting in concert to ensure robust morphogenesis have been described in several developmental systems. For instance, successful ventral furrow formation in *Drosophila* requires apical constriction, basal relaxation, and cell shortening,[67] while basal constriction in conjunction with tissue compaction caused by cell migration drives retinal neuroepithelium invagination in *Zebrafish* embryos.[68]

The nucleus is the primary site for gene regulation and genome protection. In addition, attributes such as its size, position, and stiffness and its interaction with the cytoskeleton render the nucleus a dominant physical entity within the cell. Our results suggest that friction between the nucleus and the ECM is a major impediment to cell movement. Although crawling cells and DTCs utilize distinct physical mechanisms for forward propulsion (actin polymerization at the front in crawling cells and external pressure from the gonadal bulk in the DTC), in both cases intracellular forces are required to overcome localized resistance to motion: traction forces of rear adhesions in the case of crawling cells[69] or resistance by the nucleus in the case of the DTC motion. Moreover, since myosin functions as an actin cross-linker as well as a motor,[70] its inhibition results in an impaired connectivity of the cortical network, leading to reduction of the critical tension beyond which the cell fragments. Inhibition of myosin is therefore a common mechanism that leads to elongation, deformation, and eventual break-up of motile cells under such conditions.

Our results also reveal the remarkable capability of a cytoplast to repolarize and organize its cytoskeleton to support continued invasion. To the best of our knowledge, this is the first report showing that a cytoplasmic fragment can invade and direct organ morphogenesis *in vivo*. Enucleated cells are present in several physiological contexts,[71] including erythrocytes,[72,73] cornified keratinocytes,[74] and eye lens fiber cells.[75] The elimination of the nucleus is essential for the erythrocytes to fit into the narrow blood capillaries and for keratinocytes to form a tough and water-resistant barrier, and it allows lens fiber cells to create a transparent eye lens.[71] Cytoplasts are also observed in pathological situations: for instance, neutrophil cytoplasts trigger severe asthma,[76] and circulating tumor cytoplasts formed by shear stress assist in metastasis.[77] Interestingly, cytoplasts have been genetically engineered for targeted drug delivery.[78] Given that the DTC cytoplast retains polarity, cytoskeletal architecture, and invasive behavior, it may serve as an *in vivo* model to gain further insight into the capabilities of a cell devoid of a nucleus.

STAR★METHODS

Detailed methods are provided in the online version of this paper and include the following:

- KEY RESOURCES TABLE
- RESOURCE AVAILABILITY
  - Lead contact
  - Materials availability
  - Data and code availability
- EXPERIMENTAL MODEL AND SUBJECT DETAILS
  - *C. elegans* maintenance
- METHOD DETAILS
  - RNA interference
  - Phalloidin staining
  - Immunofluorescence staining for FLAG epitope
  - Fluorescence imaging
- MICROFLUIDIC DEVICE FABRICATION
  - Device operation
  - On-chip RNAi
  - Image analysis
  - Laser ablation
- QUANTIFICATION AND STATISTICAL ANALYSIS

SUPPLEMENTAL INFORMATION

Supplemental information can be found online at https://doi.org/10.1016/j.cub.2024.03.049.

ACKNOWLEDGMENTS

This work was supported by Israel Science Foundation grants 767/20 and 3308/20 and funding from the United States - Israel Binational Science Foundation grant 2021014 awarded to R.Z.B and Israel Science Foundation grant 2751/20 awarded to T.S. We thank Alex Hajnal and Andrew deMello for their support of S.B. We thank Yakira M. Becker for the graphical abstract.

AUTHOR CONTRIBUTIONS

P.A. conceptualized the project, performed all experiments, analyzed and visualized data, and wrote the paper; S.B. provided microfluidic-based long-term imaging; T.S. contributed conceptualization and contributed to writing of the paper; R.Z.B. contributed conceptualization, obtained funding, analyzed data, and wrote the paper.

DECLARATION OF INTERESTS

The authors declare no competing interests.

Received: June 15, 2023
Revised: February 1, 2024
Accepted: March 25, 2024
Published: May 21, 2024

REFERENCES

1. Wolf, K., te Lindert, M., Krause, M., Alexander, S., te Riet, J., Willis, A.L., Hoffman, R.M., Figdor, C.G., Weiss, S.J., and Friedl, P. (2013). Physical limits of cell migration: Control by ECM space and nuclear deformation and tuning by proteolysis and traction force. J. Cell Biol. *201*, 1069–1084. https://doi.org/10.1083/jcb.201210152.

2. McGregor, A.L., Hsia, C.-R., and Lammerding, J. (2016). Squish and squeeze—the nucleus as a physical barrier during migration in confined environments. Curr. Opin. Cell Biol. *40*, 32–40. https://doi.org/10.1016/j.ceb.2016.01.011.

3. Gomes, E.R., Jani, S., and Gundersen, G.G. (2005). Nuclear movement regulated by Cdc42, MRCK, myosin, and actin flow establishes MTOC polarization in migrating cells. Cell *121*, 451–463. https://doi.org/10.1016/j.cell.2005.02.022.

4. Petrie, R.J., Koo, H., and Yamada, K.M. (2014). Generation of compartmentalized pressure by a nuclear piston governs cell motility in a 3D matrix. Science *345*, 1062–1065. https://doi.org/10.1126/science.1256965.

5. Renkawitz, J., Kopf, A., Stopp, J., de Vries, I., Driscoll, M.K., Merrin, J., Hauschild, R., Welf, E.S., Danuser, G., Fiolka, R., and Sixt, M. (2019). Nuclear positioning facilitates amoeboid migration along the path of least resistance. Nature *568*, 546–550. https://doi.org/10.1038/s41586-019-1087-5.

6. Barzilai, S., Yadav, S.K., Morrell, S., Roncato, F., Klein, E., Stoler-Barak, L., Golani, O., Feigelson, S.W., Zemel, A., Nourshargh, S., and Alon, R. (2017). Leukocytes breach endothelial barriers by insertion of nuclear lobes and disassembly of endothelial actin filaments. Cell Rep. *18*, 685–699. https://doi.org/10.1016/j.celrep.2016.12.076.

7. Gundersen, G.G., and Worman, H.J. (2013). Nuclear Positioning. Cell *152*, 1376–1389. https://doi.org/10.1016/j.cell.2013.02.031.

8. Deshpande, O., and Telley, I.A. (2021). Nuclear positioning during development: Pushing, pulling and flowing. Semin. Cell Dev. Biol. *120*, 10–21. https://doi.org/10.1016/j.semcdb.2021.09.020.

9. Bone, C.R., and Starr, D.A. (2016). Nuclear migration events throughout development. J. Cell Sci. *129*, 1951–1961. https://doi.org/10.1242/jcs.179788.

10. Lee, Y.L., and Burke, B. (2018). LINC complexes and nuclear positioning. Semin. Cell Dev. Biol. *82*, 67–76. https://doi.org/10.1016/j.semcdb.2017.11.008.

11. Bouzid, T., Kim, E., Riehl, B.D., Esfahani, A.M., Rosenbohm, J., Yang, R., Duan, B., and Lim, J.Y. (2019). The LINC complex, mechanotransduction, and mesenchymal stem cell function and fate. J. Biol. Eng. *13*, 68. https://doi.org/10.1186/s13036-019-0197-9.

12. Maurer, M., and Lammerding, J. (2019). The Driving Force: Nuclear Mechanotransduction in Cellular Function, Fate, and Disease. Annu. Rev. Biomed. Eng. *21*, 443–468. https://doi.org/10.1146/annurev-bioeng-060418-052139.

13. Zhou, C., Rao, L., Warren, D.T., Shanahan, C.M., and Zhang, Q. (2018). Mouse models of nesprin-related diseases. Biochem. Soc. Trans. *46*, 669–681. https://doi.org/10.1042/BST20180085.

14. Banerjee, I., Zhang, J., Moore-Morris, T., Pfeiffer, E., Buchholz, K.S., Liu, A., Ouyang, K., Stroud, M.J., Gerace, L., Evans, S.M., et al. (2014). Targeted Ablation of Nesprin 1 and Nesprin 2 from Murine Myocardium Results in Cardiomyopathy, Altered Nuclear Morphology and Inhibition of the Biomechanical Gene Response. PLoS Genet. *10*, e1004114. https://doi.org/10.1371/journal.pgen.1004114.

15. Kim, H.-S., Murakami, R., Quintin, S., Mori, M., Ohkura, K., Tamai, K.K., Labouesse, M., Sakamoto, H., and Nishiwaki, K. (2011). VAB-10 spectraplakin acts in cell and nuclear migration in *Caenorhabditis elegans*. Development *138*, 4013–4023. https://doi.org/10.1242/dev.059568.

16. Kimble, J., and Crittenden, S.L. (2005). Germline proliferation and its control. WormBook. 1–14. https://doi.org/10.1895/wormbook.1.13.1.

17. Kershner, A.M., Shin, H., Hansen, T.J., and Kimble, J. (2014). Discovery of two GLP-1/Notch target genes that account for the role of GLP-1/Notch signaling in stem cell maintenance*111*, pp. 3739–3744. https://doi.org/10.1073/pnas.1401861111.

18. Agarwal, P., Shemesh, T., and Zaidel-Bar, R. (2022). Directed cell invasion and asymmetric adhesion drive tissue elongation and turning in C. elegans gonad morphogenesis. Dev. Cell *57*, 2111–2126.e6. https://doi.org/10.1016/j.devcel.2022.08.003.

19. Chan, S.S., Zheng, H., Su, M.W., Wilk, R., Killeen, M.T., Hedgecock, E.M., and Culotti, J.G. (1996). UNC-40, a C. elegans homolog of DCC (Deleted in Colorectal Cancer), is required in motile cells responding to UNC-6 netrin cues. Cell *87*, 187–195. https://doi.org/10.1016/s0092-8674(00)81337-9.

20. Hedgecock, E.M., Culotti, J.G., and Hall, D.H. (1990). The unc-5, unc-6, and unc-40 genes guide circumferential migrations of pioneer axons and mesodermal cells on the epidermis in C. elegans. Neuron *4*, 61–85. https://doi.org/10.1016/0896-6273(90)90444-K.

21. Leung-Hagesteijn, C., Spence, A.M., Stern, B.D., Zhou, Y., Su, M.W., Hedgecock, E.M., and Culotti, J.G. (1992). UNC-5, a transmembrane protein with immunoglobulin and thrombospondin type 1 domains, guides cell and pioneer axon migrations in C. elegans. Cell *71*, 289–299. https://doi.org/10.1016/0092-8674(92)90357-i.

22. Sherwood, D.R., and Plastino, J. (2018). Invading, Leading and Navigating Cells in Caenorhabditis elegans : Insights into Cell Movement in Vivo. Genetics *208*, 53–78. https://doi.org/10.1534/genetics.117.300082.

23. Malone, C.J., Fixsen, W.D., Horvitz, H.R., and Han, M. (1999). UNC-84 localizes to the nuclear envelope and is required for nuclear migration and anchoring during C. elegans development. Development *126*, 3171–3181. https://doi.org/10.1242/dev.126.14.3171.

24. Starr, D.A., Hermann, G.J., Malone, C.J., Fixsen, W., Priess, J.R., Horvitz, H.R., and Han, M. (2001). unc-83 encodes a novel component of the nuclear envelope and is essential for proper nuclear migration. Development *128*, 5039–5050. https://doi.org/10.1242/dev.128.24.5039.

25. McGee, M.D., Rillo, R., Anderson, A.S., and Starr, D.A. (2006). UNC-83 Is a KASH Protein Required for Nuclear Migration and Is Recruited to the Outer Nuclear Membrane by a Physical Interaction with the SUN Protein UNC-84. MBoC *17*, 1790–1801. https://doi.org/10.1091/mbc.e05-09-0894.

26. Starr, D.A., and Fischer, J.A. (2005). KASH 'n Karry: The KASH domain family of cargo-specific cytoskeletal adaptor proteins. Bioessays *27*, 1136–1146. https://doi.org/10.1002/bies.20312.

27. Sulston, J.E., and Horvitz, H.R. (1981). Abnormal cell lineages in mutants of the nematode Caenorhabditis elegans. Dev. Biol. *82*, 41–55. https://doi.org/10.1016/0012-1606(81)90427-9.

28. Horvitz, H.R., and Sulston, J.E. (1980). ISOLATION AND GENETIC CHARACTERIZATION OF CELL-LINEAGE MUTANTS OF THE NEMATODE *CAENORHABDITIS ELEGANS*. Genetics *96*, 435–454. https://doi.org/10.1093/genetics/96.2.435.

29. Hedgecock, E.M., and Thomson, J.N. (1982). A gene required for nuclear and mitochondrial attachment in the nematode Caenorhabditis elegans. Cell *30*, 321–330. https://doi.org/10.1016/0092-8674(82)90038-1.

30. Hao, H., Kalra, S., Jameson, L.E., Guerrero, L.A., Cain, N.E., Bolivar, J., and Starr, D.A. (2021). The Nesprin-1/-2 ortholog ANC-1 regulates organelle positioning in C. elegans independently from its KASH or actin-binding domains. Elife *10*, e61069. https://doi.org/10.7554/eLife.61069.

31. Starr, D.A. (2019). A network of nuclear envelope proteins and cytoskeletal force generators mediates movements of and within nuclei throughout *Caenorhabditis elegans* development. Exp. Biol. Med. *244*, 1323–1332. https://doi.org/10.1177/1535370219871965.

32. Starr, D.A., and Han, M. (2002). Role of ANC-1 in tethering nuclei to the actin cytoskeleton. Science *298*, 406–409. https://doi.org/10.1126/science.1075119.

33. Cain, N.E., Jahed, Z., Schoenhofen, A., Valdez, V.A., Elkin, B., Hao, H., Harris, N.J., Herrera, L.A., Woolums, B.M., Mofrad, M.R.K., et al. (2018). Conserved SUN-KASH interfaces mediate LINC complex-dependent nuclear movement and positioning. Curr. Biol. *28*, 3086–3097.e4. https://doi.org/10.1016/j.cub.2018.08.001.

34. Meyerzon, M., Fridolfsson, H.N., Ly, N., McNally, F.J., and Starr, D.A. (2009). UNC-83 is a nuclear-specific cargo adaptor for kinesin-1-mediated nuclear migration. Development *136*, 2725–2733. https://doi.org/10.1242/dev.038596.

35. Fridolfsson, H.N., Ly, N., Meyerzon, M., and Starr, D.A. (2010). UNC-83 coordinates kinesin-1 and dynein activities at the nuclear envelope during

nuclear migration. Dev. Biol. *338*, 237–250. https://doi.org/10.1016/j.ydbio.2009.12.004.

36. Fridolfsson, H.N., and Starr, D.A. (2010). Kinesin-1 and dynein at the nuclear envelope mediate the bidirectional migrations of nuclei. J. Cell Biol. *191*, 115–128. https://doi.org/10.1083/jcb.201004118.

37. Bone, C.R., Chang, Y.-T., Cain, N.E., Murphy, S.P., and Starr, D.A. (2016). Nuclei migrate through constricted spaces using microtubule motors and actin networks in C. elegans hypodermal cells. Development *143*, 4193–4202. https://doi.org/10.1242/dev.141192.

38. Lawrence, K.S., Tapley, E.C., Cruz, V.E., Li, Q., Aung, K., Hart, K.C., Schwartz, T.U., Starr, D.A., and Engebrecht, J. (2016). LINC complexes promote homologous recombination in part through inhibition of nonhomologous end joining. J. Cell Biol. *215*, 801–821. https://doi.org/10.1083/jcb.201604112.

39. Sosa, B.A., Rothballer, A., Kutay, U., and Schwartz, T.U. (2012). LINC complexes form by binding of three KASH peptides to domain interfaces of trimeric SUN proteins. Cell *149*, 1035–1047. https://doi.org/10.1016/j.cell.2012.03.046.

40. Tapley, E.C., and Starr, D.A. (2013). Connecting the nucleus to the cytoskeleton by SUN–KASH bridges across the nuclear envelope. Curr. Opin. Cell Biol. *25*, 57–62. https://doi.org/10.1016/j.ceb.2012.10.014.

41. Berger, S., Spiri, S., deMello, A., and Hajnal, A. (2021). Microfluidic-based imaging of complete Caenorhabditis elegans larval development. Development *148*, dev199674. https://doi.org/10.1242/dev.199674.

42. Kimble, J., and Crittenden, S.L. (2007). Controls of Germline Stem Cells, Entry into Meiosis, and the Sperm/Oocyte Decision in *Caenorhabditis elegans*. Annu. Rev. Cell Dev. Biol. *23*, 405–433. https://doi.org/10.1146/annurev.cellbio.23.090506.123326.

43. Hong, Y., Roy, R., and Ambros, V. (1998). Developmental regulation of a cyclin-dependent kinase inhibitor controls postembryonic cell cycle progression in *Caenorhabditis elegans*. Development *125*, 3585–3597. https://doi.org/10.1242/dev.125.18.3585.

44. Fay, D.S., Keenan, S., and Han, M. (2002). *fzr-1* and *lin-35* /Rb function redundantly to control cell proliferation in *C. elegans* as revealed by a nonbiased synthetic screen. Genes Dev. *16*, 503–517. https://doi.org/10.1101/gad.952302.

45. Kidd, A.R., Miskowski, J.A., Siegfried, K.R., Sawa, H., and Kimble, J. (2005). A β-Catenin Identified by Functional Rather Than Sequence Criteria and Its Role in Wnt/MAPK Signaling. Cell *121*, 761–772. https://doi.org/10.1016/j.cell.2005.03.029.

46. Asahina, M., Valenta, T., Silhankova, M., Korinek, V., and Jindra, M. (2006). Crosstalk between a Nuclear Receptor and β-Catenin Signaling Decides Cell Fates in the C. elegans Somatic Gonad. Dev. Cell *11*, 203–211. https://doi.org/10.1016/j.devcel.2006.06.003.

47. Verkhovsky, A.B., Svitkina, T.M., and Borisy, G.G. (1999). Self-polarization and directional motility of cytoplasm. Curr. Biol. *9*, 11–20. https://doi.org/10.1016/s0960-9822(99)80042-6.

48. Cai, Y., Rossier, O., Gauthier, N.C., Biais, N., Fardin, M.-A., Zhang, X., Miller, L.W., Ladoux, B., Cornish, V.W., and Sheetz, M.P. (2010). Cytoskeletal coherence requires myosin-IIA contractility. J. Cell Sci. *123*, 413–423. https://doi.org/10.1242/jcs.058297.

49. Kozlov, M.M., and Mogilner, A. (2007). Model of polarization and bistability of cell fragments. Biophys. J. *93*, 3811–3819. https://doi.org/10.1529/biophysj.107.110411.

50. Blelloch, R., Anna-Arriola, S.S., Gao, D., Li, Y., Hodgkin, J., and Kimble, J. (1999). The gon-1 Gene Is Required for Gonadal Morphogenesis in Caenorhabditis elegans. Dev. Biol. *216*, 382–393. https://doi.org/10.1006/dbio.1999.9491.

51. Somerville, R.P.T., Longpre, J.-M., Jungers, K.A., Engle, J.M., Ross, M., Evanko, S., Wight, T.N., Leduc, R., and Apte, S.S. (2003). Characterization of ADAMTS-9 and ADAMTS-20 as a distinct ADAMTS subfamily related to Caenorhabditis elegans GON-1. J. Biol. Chem. *278*, 9503–9513. https://doi.org/10.1074/jbc.M211009200.

52. Kimble, J.E., and White, J.G. (1981). On the control of germ cell development in Caenorhabditis elegans. Dev. Biol. *81*, 208–219. https://doi.org/10.1016/0012-1606(81)90284-0.

53. Kocsisova, Z., Kornfeld, K., and Schedl, T. (2019). Rapid, population-wide declines in stem cell number and activity during reproductive aging in *C. elegans*. Development, dev. *146*, 173195. https://doi.org/10.1242/dev.173195.

54. Lee, C., Sorensen, E.B., Lynch, T.R., and Kimble, J. (2016). C. elegans GLP-1/Notch activates transcription in a probability gradient across the germline stem cell pool. Elife *5*, e18370. https://doi.org/10.7554/eLife.18370.

55. Shin, H., Haupt, K.A., Kershner, A.M., Kroll-Conner, P., Wickens, M., and Kimble, J. (2017). SYGL-1 and LST-1 link niche signaling to PUF RNA repression for stem cell maintenance in Caenorhabditis elegans. PLoS Genet. *13*, e1007121. https://doi.org/10.1371/journal.pgen.1007121.

56. Sugioka, K., Fielmich, L.-E., Mizumoto, K., Bowerman, B., van den Heuvel, S., Kimura, A., and Sawa, H. (2018). Tumor suppressor APC is an attenuator of spindle-pulling forces during C. elegans asymmetric cell division*115*, pp. E954–E963. https://doi.org/10.1073/pnas.1712052115.

57. Srayko, M., Kaya, A., Stamford, J., and Hyman, A.A. (2005). Identification and Characterization of Factors Required for Microtubule Growth and Nucleation in the Early C. elegans Embryo. Dev. Cell *9*, 223–236. https://doi.org/10.1016/j.devcel.2005.07.003.

58. Chuang, C.-H., Schlientz, A.J., Yang, J., and Bowerman, B. (2020). Microtubule assembly and pole coalescence: early steps in *C. elegans* oocyte meiosis I spindle assembly. Biol. Open *9*, bio052308. https://doi.org/10.1242/bio.052308.

59. Ho, J., Venecia, A.V., Ma, L., and Starr, D.A. (2018). Characterizing Dynein's Role in P-cell Nuclear Migration using an Auxin-Induced Degradation System. MicroPubl Biol. *2018*. https://doi.org/10.17912/W2W96J.

60. Khalilgharibi, N., Fouchard, J., Asadipour, N., Barrientos, R., Duda, M., Bonfanti, A., Yonis, A., Harris, A., Mosaffa, P., Fujita, Y., et al. (2019). Stress relaxation in epithelial monolayers is controlled by the actomyosin cortex. Nat. Phys. *15*, 839–847. https://doi.org/10.1038/s41567-019-0516-6.

61. Lautscham, L.A., Kämmerer, C., Lange, J.R., Kolb, T., Mark, C., Schilling, A., Strissel, P.L., Strick, R., Gluth, C., Rowat, A.C., et al. (2015). Migration in confined 3D environments is determined by a combination of adhesiveness, nuclear volume, contractility, and cell stiffness. Biophys. J. *109*, 900–913. https://doi.org/10.1016/j.bpj.2015.07.025.

62. Lomakin, A.J., Cattin, C.J., Cuvelier, D., Alraies, Z., Molina, M., Nader, G.P.F., Srivastava, N., Sáez, P.J., Garcia-Arcos, J.M., Zhitnyak, I.Y., et al. (2020). The nucleus acts as a ruler tailoring cell responses to spatial constraints. Science *370*, eaba2894. https://doi.org/10.1126/science.aba2894.

63. Smith, A.S., Nowak, R.B., Zhou, S., Giannetto, M., Gokhin, D.S., Papoin, J., Ghiran, I.C., Blanc, L., Wan, J., and Fowler, V.M. (2018). Myosin IIA interacts with the spectrin-actin membrane skeleton to control red blood cell membrane curvature and deformability*115*, pp. E4377–E4385. https://doi.org/10.1073/pnas.1718285115.

64. Diz-Muñoz, A., Fletcher, D.A., and Weiner, O.D. (2013). Use the force: membrane tension as an organizer of cell shape and motility. Trends Cell Biol. *23*, 47–53. https://doi.org/10.1016/j.tcb.2012.09.006.

65. Olbrich, K., Rawicz, W., Needham, D., and Evans, E. (2000). Water Permeability and Mechanical Strength of Polyunsaturated Lipid Bilayers. Biophys. J. *79*, 321–327. https://doi.org/10.1016/S0006-3495(00)76294-1.

66. Li, F., Chan, C.U., and Ohl, C.D. (2013). Yield strength of human erythrocyte membranes to impulsive stretching. Biophys. J. *105*, 872–879. https://doi.org/10.1016/j.bpj.2013.06.045.

67. Krueger, D., Tardivo, P., Nguyen, C., and De Renzis, S. (2018). Downregulation of basal myosin-II is required for cell shape changes and tissue invagination. The EMBO journal *37*, e100170. https://doi.org/10.15252/embj.2018100170.

68. Sidhaye, J., and Norden, C. (2017). Concerted action of neuroepithelial basal shrinkage and active epithelial migration ensures efficient optic cup morphogenesis. Elife *6*, e22689. https://doi.org/10.7554/eLife.22689.

69. Poincloux, R., Collin, O., Lizárraga, F., Romao, M., Debray, M., Piel, M., and Chavrier, P. (2011). Contractility of the cell rear drives invasion of breast tumor cells in 3D Matrigel. Proc. Natl. Acad. Sci. USA *108*, 1943–1948. https://doi.org/10.1073/pnas.1010396108.

70. Laevsky, G., and Knecht, D.A. (2003). Cross-linking of actin filaments by myosin II is a major contributor to cortical integrity and cell motility in restrictive environments. J. Cell Sci. *116*, 3761–3770. https://doi.org/10.1242/jcs.00684.

71. Rogerson, C., Bergamaschi, D., and O'Shaughnessy, R.F.L. (2018). Uncovering mechanisms of nuclear degradation in keratinocytes: A paradigm for nuclear degradation in other tissues. Nucleus *9*, 56–64. https://doi.org/10.1080/19491034.2017.1412027.

72. Migliaccio, A.R. (2010). Erythroblast enucleation. Haematologica *95*, 1985–1988. https://doi.org/10.3324/haematol.2010.033225.

73. Ji, P. (2015). New insights into the mechanisms of mammalian erythroid chromatin condensation and enucleation. Int. Rev. Cell Mol. Biol. *316*, 159–182. https://doi.org/10.1016/bs.ircmb.2015.01.006.

74. Eckhart, L., Lippens, S., Tschachler, E., and Declercq, W. (2013). Cell death by cornification. Biochim. Biophys. Acta *1833*, 3471–3480. https://doi.org/10.1016/j.bbamcr.2013.06.010.

75. Bassnett, S. (2009). On the mechanism of organelle degradation in the vertebrate lens. Exp. Eye Res. *88*, 133–139. https://doi.org/10.1016/j.exer.2008.08.017.

76. Krishnamoorthy, N., Douda, D.N., Brüggemann, T.R., Ricklefs, I., Duvall, M.G., Abdulnour, R.-E.E., Martinod, K., Tavares, L., Wang, X., Cernadas, M., et al. (2018). Neutrophil cytoplasts induce TH17 differentiation and skew inflammation toward neutrophilia in severe asthma. Sci. Immunol. *3*, eaao4747. https://doi.org/10.1126/sciimmunol.aao4747.

77. Headley, M.B., Bins, A., Nip, A., Roberts, E.W., Looney, M.R., Gerard, A., and Krummel, M.F. (2016). Visualization of immediate immune responses to pioneer metastatic cells in the lung. Nature *531*, 513–517. https://doi.org/10.1038/nature16985.

78. Wang, H., Alarcón, C.N., Liu, B., Watson, F., Searles, S., Lee, C.K., Keys, J., Pi, W., Allen, D., Lammerding, J., et al. (2022). Genetically engineered and enucleated human mesenchymal stromal cells for the targeted delivery of therapeutics to diseased tissue. Nat. Biomed. Eng. *6*, 882–897. https://doi.org/10.1038/s41551-021-00815-9.

79. Linden, L.M., Gordon, K.L., Pani, A.M., Payne, S.G., Garde, A., Burkholder, D., Chi, Q., Goldstein, B., and Sherwood, D.R. (2017). Identification of regulators of germ stem cell enwrapment by its niche in C. elegans. Dev. Biol. *429*, 271–284. https://doi.org/10.1016/j.ydbio.2017.06.019.

80. Heppert, J.K., Dickinson, D.J., Pani, A.M., Higgins, C.D., Steward, A., Ahringer, J., Kuhn, J.R., and Goldstein, B. (2016). Comparative assessment of fluorescent proteins for in vivo imaging in an animal model system. Mol. Biol. Cell *27*, 3385–3394. https://doi.org/10.1091/mbc.E16-01-0063.

81. Haithcock, E., Dayani, Y., Neufeld, E., Zahand, A.J., Feinstein, N., Mattout, A., Gruenbaum, Y., and Liu, J. (2005). Age-related changes of nuclear architecture in Caenorhabditis elegans *102*, pp. 16690–16695. https://doi.org/10.1073/pnas.0506955102.

82. Zhang, Y., Yang, Y., Zhu, Z., and Ou, G. (2017). WASP-Arp2/3-dependent actin polymerization influences fusogen localization during cell-cell fusion in C. elegans embryos. Biol. Open *6*, 1324–1328. https://doi.org/10.1242/bio.026807.

83. Walser, M., Umbricht, C.A., Fröhli, E., Nanni, P., and Hajnal, A. (2017). β-Integrin de-phosphorylation by the Density-Enhanced Phosphatase DEP-1 attenuates EGFR signaling in C. elegans. PLoS Genet. *13*, e1006592. https://doi.org/10.1371/journal.pgen.1006592.

84. Keeley, D.P., Hastie, E., Jayadev, R., Kelley, L.C., Chi, Q., Payne, S.G., Jeger, J.L., Hoffman, B.D., and Sherwood, D.R. (2020). Comprehensive Endogenous Tagging of Basement Membrane Components Reveals Dynamic Movement within the Matrix Scaffolding. Dev. Cell *54*, 60–74.e7. https://doi.org/10.1016/j.devcel.2020.05.022.

85. Schindelin, J., Arganda-Carreras, I., Frise, E., Kaynig, V., Longair, M., Pietzsch, T., Preibisch, S., Rueden, C., Saalfeld, S., Schmid, B., et al. (2012). Fiji: an open-source platform for biological-image analysis. Nat. Methods *9*, 676–682. https://doi.org/10.1038/nmeth.2019.

86. Brenner, S. (1974). The genetics of Caenorhabditis elegans. Genetics *77*, 71–94. https://doi.org/10.1093/genetics/77.1.71.

87. Timmons, L. (2006). Delivery methods for RNA interference in C. elegans. Methods Mol. Biol. *351*, 119–125. https://doi.org/10.1385/1-59745-151-7:119.

88. Sturm, Á., Saskoi, É., Tibor, K., Weinhardt, N., and Vellai, T. (2018). Highly efficient RNAi and Cas9-based auto-cloning systems for C. elegans research. Nucleic Acids Res. *46*, e105. https://doi.org/10.1093/NAR/GKY516.

89. Kamath, R.S., and Ahringer, J. (2003). Genome-wide RNAi screening in Caenorhabditis elegans. Methods (San Diego, Calif.) *30*, 313–321. https://doi.org/10.1016/S1046-2023(03)00050-1.

90. Rual, J.-F., Ceron, J., Koreth, J., Hao, T., Nicot, A.-S., Hirozane-Kishikawa, T., Vandenhaute, J., Orkin, S.H., Hill, D.E., van den Heuvel, S., and Vidal, M. (2004). Toward Improving *Caenorhabditis elegans* Phenome Mapping With an ORFeome-Based RNAi Library. Genome Res. *14*, 2162–2168. https://doi.org/10.1101/gr.2505604.

91. Xia, Y., and Whitesides, G.M. (1998). SOFT LITHOGRAPHY. Annu. Rev. Mater. Sci. *28*, 153–184. https://doi.org/10.1146/annurev.matsci.28.1.153.

92. Unger, M.A., Chou, H.-P., Thorsen, T., Scherer, A., and Quake, S.R. (2000). Monolithic Microfabricated Valves and Pumps by Multilayer Soft Lithography. Science *288*, 113–116. https://doi.org/10.1126/science.288.5463.113.

93. Driscoll, M.K., McCann, C., Kopace, R., Homan, T., Fourkas, J.T., Parent, C., and Losert, W. (2012). Cell shape dynamics: from waves to migration. PLoS Comput. Biol. *8*, e1002392. https://doi.org/10.1371/journal.pcbi.1002392.

Please cite this article in press as: Agarwal et al., Active nuclear positioning and actomyosin contractility maintain leader cell integrity during gonadogenesis, Current Biology (2024), https://doi.org/10.1016/j.cub.2024.03.049

STAR★METHODS

KEY RESOURCES TABLE

REAGENT or RESOURCE	SOURCE	IDENTIFIER
Antibodies		
Anti-FLAG M2 antibody	Sigma	Cat # F1804; RRID: AB_262044
Alexa Fluor 488-conjugated goat anti-mouse IgG	Abcam	Cat # ab150113; RRID: AB_2576208
Bacterial and virus strains		
E. coli OP50	*Caenorhabditis Genetics Center* (CGC)	OP50
HT115 (DE3)	*Caenorhabditis Genetics Center* (CGC)	OP50
E. coli: Ahringer and Vidal RNAi library	Source Bioscience	*C. elegans* RNAi collection
Chemicals, peptides, and recombinant proteins		
Chlorotrimethylsilane	Sigma Aldrich	89595
DAPI	Santa Cruz Biotechnology	SC-3598
IPTG	Gold Biocom	I2481C100
Optiprep	Sigma Aldrich	D1556
PDMS - Elastosil RT601 A/B	Ameba	60080682 A/B
Alexa Fluor™ 568 Phalloidin	Thermo Fisher Scientific	A12380
SU8 photoresist GM1050	Gersteltec	GM1050
SU8 photoresist GM1060	Gersteltec	GM1060
Silicon wafers	Siegert Wafer	4P0/>1/525 ± 25/SSP/TTV<10
Pluronic F127	Sigma Aldrich	P2443
Propylene glycol methyl ether acetate PGMEA	Sigma Aldrich	484431
10X PBS	Hylab	BP507/500D
Ampicillin	Formedium	AMP100
Levamisole	Sigma	L9756-5G
Triton X-100	Sigma	X100-100ML
Tween 20	Sigma	P1379-100ML
BSA	VWR Life Science	97061–420
Formaldehyde	BioLab	06750523
Methanol	BioLab	001368350100
Glycine	BioLab	000713239100
Agarose	SeaKem LE	50004
Chlorotrimethyl silane	Sigma	92361
Vectashield	Vector Laboratories	H-1200
Experimental models: Organisms/strains		
cpIs121 I; rrf-3(pk1426) II; rde-1(ne219) V	Linden et al.[79]	NK2115
cpIs121 I; rrf-3(pk1426) II; rde-1(ne219) V;ltIs44 [Ppie-1::mCherry::PH(PLC1delta1); unc-119(+)] IV	Agarwal et al.[18]	RZB353
mig-24p::Venus	Kiyoji Nishiwaki lab	NF2169
mig-24p::SKI-Lodge casette::WrmScarlet	Agarwal et al.[18]	RZB350
cpIs121 I; rrf-3(pk1426) II; rde-1(ne219) V;tba-1 ((knu639 [pNU1541 - N-terminal degron mKate2 unc-119(+)] unc-119(ed3) III))I	Agarwal et al.[18]	RZB354
unc-83(yc26[unc-83::gfp::kash+LoxP])V	Bone et al.[37]	UD473
unc-84(yc24[unc-84::gfp+LoxP])X	Lawrence et al.[38]	UD476
mig-24p::SKI-Lodge casette::WrmScarlet; unc-83(yc26[unc-83::gfp::kash+LoxP])V/+	This study	RZB386
mig-24p::SKI-Lodge casette::WrmScarlet; unc-84(yc24[unc-84::gfp+LoxP])X	This study	RZB387

(*Continued on next page*)

Please cite this article in press as: Agarwal et al., Active nuclear positioning and actomyosin contractility maintain leader cell integrity during gonadogenesis, Current Biology (2024), https://doi.org/10.1016/j.cub.2024.03.049

Continued

REAGENT or RESOURCE	SOURCE	IDENTIFIER
anc-1(yc68[GFP::anc-1b])	Hao et al.[30]	UD612
mig-24p::SKI-Lodge casette::WrmScarlet; anc-1(yc68[GFP::anc-1b])	This study	RZB491
nmy-2(cp52 [nmy-2::kate + LoxP unc-119(+) LoxP]) I; unc-119 (ed3) III	Heppert et al.[80]	LP229
qIs56 [lag-2p::GFP + unc-119(+)]; nmy-2 (cp52[nmy-2::mkate]) I	This study	RZB326
ccIs4810 [(pJKL380.4) *lmn-1p::lmn-1::GFP::lmn-1* 3′utr + (pMH86) dpy-20(+)] I	Haithcock E et al.[81]	LW697
cpIs121 I; rrf-3(pk1426) II; rde-1(ne219) V;tba-1 ((knu639 [pNU1541 - N-terminal degron mKate2 unc-119(+)] unc-119(ed3) III))I; ccIs4810 [(pJKL380.4) *lmn-1p::lmn-1::GFP::lmn-1* 3′utr + (pMH86) *dpy-20*(+)] I	This study	RZB418
cas725 [arx-2::TagRFP knock-in]	Zhang et al.[82]	GOU2905
pat-3(zh115[gfp::pat-3]) I.	Alex Hajnal lab	AH4617
tln-1(zh117[gfp::tln-1]) I.	Walser et al.[83]	AH3437
tln-1(zh117[gfp::tln-1]) I; cas725 [arx-2::TagRFP knock-in]	This study	RZB376
gon-1(qy45[gon-1::mNG+loxP]) IV.	Keeley et al.[84]	NK2590
rrf-3(pk1426); pat-3::GFP; mig-24p:: SKI-Lodge casette::WrmScarlet	Agarwal et al.[18]	RZB392
mig-24p::SKI-Lodge casette::WrmScarlet;qyIs108 [lam- 1p::lam-1::dendra +unc-119(+)]	Agarwal et al.[18]	RZB422
sygl-1(am307[3xFLAG::sygl-1]) I	Kocsisova Z et al.[53]	WU1770
cpIs121 I; rrf-3(pk1426) II; rde-1(ne219) V; sygl-1(am307[3xFLAG::sygl-1]) I	This study	RZB394
tac-1(or1955[gfp::tac-1]) II; ltIs37 IV	Chuang CH et al.[58]	EU3121
zyg-9(or1956[gfp::zyg-9]) II; ltIs37 IV	Chuang CH et al.[58]	EU3169
ebp-2(or1954[ebp-2::mKate2]) II; ruIs57	Sugioka K et al.[56]	EU3068
mig-24p::SKI-Lodge casette::WrmScarlet;ina-1 (qy23[ina-1::mNG]) III	Agarwal et al.[18]	RZB423
Recombinant DNA		
Plasmid L4440	Addgene	#1654
Plasmid T444T	Addgene	#113081
Software and algorithms		
Adobe Illustrator	Adobe	https://www.adobe.com
Fiji	Schindelin et al.[85]	http://fiji.sc/
GraphPad Prism	GraphPad Software	https://www.graphpad.com
MATLAB	MathWorks	https://ch.mathworks.com/products/matlab.html
Metamorph	Molecular devices	7.10.2.240
Other		
1/16″ tygon tubing	Thermo Fisher Scientific	15157044
1/32″ tygon tubing	Thermo Fisher Scientific	15137044
23G hollow steel pins	Gonano Dosiertechnik	IP7R23050
23G blunt needles	Gonano Dosiertechnik	GGA723050
30G blunt needles	Gonano Dosiertechnik	IP730050
10 μm filter	pluriSelect	pluriStrainer Mini 10 μm
High-resolution film mask	Micro Lithography Services Ltd	N/A
Silicon Wafer	Siegert Wafer	4P0/>1/525 ± 25/SSP/TTV<10
Cover glass 50 × 24mm	Hecht assistant, Germany	41014551
20G Catheter Punch	SYNEO	CR0350255N20R4
Syringe Pump	World Precision Instruments	AL-1000

(*Continued on next page*)

Continued

REAGENT or RESOURCE	SOURCE	IDENTIFIER
1 mL Syringe	Fisher Scientific	11338763
Solenoid	Distrelec	154-22-898
Solenoid Base	Distrelec	154-22-899
Cable	Distrelec	143-46-643
M5 to 6mm push-in adapter	Distrelec	110-30-131
M5 to 4mm push-in adapter	Distrelec	110-30-128
Nylon-Luer-Fitting	Fisher Scientific	11776048
6mm Polyurethane tubing	Angst+Pfister	1201150604
4mm Polyurethane tubing	Angst+Pfister	1201150402
Manometer	Distrelec	154-23-643
Pressure regulator	Distrelec	154-23-579
G1/4 to 6mm push-in adapter	Distrelec	301-69-323
Air plasma	Zepto Plasma cleaner	N/A
Elastosil RT601	Ameba	60080682
Mask aligner	Kloe	UV-KUB3
iLAS Pulse system	GATACA Systems	N/A
Microscope	Nikon	Ti2E
Spinning disk confocal	Yokogawa	CSU-W1
sCMOS camera	Photometrics	Prime 95B
Microscope objective	Nikon	60X and 100X oil immersion Plan-Apochromat objective

RESOURCE AVAILABILITY

Lead contact

Further information and requests for resources and reagents should be directed to and will be fulfilled by the lead contact, Ronen Zaidel-Bar (zaidelbar@tauex.tau.ac.il).

Materials availability

All the *C. elegans* strains and resources used in this study will be available upon request with the lead contact.

Data and code availability

- Raw microscopy data reported in this paper will be available upon request with the lead contact.
- This paper does not report original code.
- Any additional information required to reanalyze the data reported in this paper are available upon request from the lead contact.

EXPERIMENTAL MODEL AND SUBJECT DETAILS

C. elegans maintenance

All strains used in this study were grown on plates containing nematode growth media (NGM) seeded with OP50, an *E. coli* strain, at 20°C.[86] The genotypes of the strains used or generated for this study are detailed in the Key Resource Table.

METHOD DETAILS

RNA interference

RNAi experiments were conducted by using the standard feeding protocol.[87] For RNAi, HT115 bacterial clones expressing dsRNA, against specific genes, were obtained either from the Ahringer or Vidal RNAi library. For some of the genes, RNAi clones were not available from either library. These genes were amplified from wild-type genomic DNA, cloned into the T444T plasmid,[88] and then the plasmid was transformed into HT115 bacteria. RNAi bacterial culture grown overnight was diluted to 1:100 and grown again at 37°C until it reached an OD of 0.5. Then, the culture was induced with 10 mM IPTG for 3 h. After induction, the culture was spread

Please cite this article in press as: Agarwal et al., Active nuclear positioning and actomyosin contractility maintain leader cell integrity during gonadogenesis, Current Biology (2024), https://doi.org/10.1016/j.cub.2024.03.049

on NGM plates containing 100 μg/mL ampicillin and 1 mM IPTG. To enhance the RNAi efficiency of UNC-84, we added 100 mM IPTG to the RNAi plates after spreading the bacterial culture. Gravid adult worms were kept on the RNAi plates and allowed to lay embryos for 2 h. Later, the adult worms were removed from the RNAi plates, and after 48 h, i.e. at the L4 stage, the phenotype of the progeny was scored. HT115 bacteria containing empty L4440 plasmid (for the RNAi clones obtained from Ahringer[89] or Vidal RNAi library[90]) or empty T444T plasmid (for the RNAi clones obtained by cloning genes into T444T plasmid) was used as control. For double knockdown conditions, worms were grown on equal ratio of the bacteria containing the two RNAi clones.

Phalloidin staining

Synchronized worms at appropriate stage (50–100) were washed with PBS buffer and then decapitated in 0.5mM levamisole using a syringe needle to extrude the gonads out of the worm body. Extruded gonads were fixed with 3.5% formaldehyde for 20 min. After fixation, gonads were washed thrice with 1X PBS and then incubated for 5 min in 1X PBS containing 0.025% Triton X-100 for permeabilization. Fixed and permeabilized gonads were stained with TRITC-phalloidin and DAPI (4′,6-diamidino-2-phenylindole dihydrochloride, 1:1000) for 20 min in the dark. After staining, gonads were washed thrice with 1X PBS and mounted on 3% agarose pad with a few microliters of Vectashield mounting medium (Vector Laboratories, H-1200) for imaging.

Immunofluorescence staining for FLAG epitope

Synchronized appropriate stage worms (50–100) were washed with PBS buffer and then decapitated in 0.5mM levamisole using a syringe needle to extrude the gonads out of the worm body. Fixation and staining was carried out as described previously.[53] Extruded gonads were fixed with 4% formaldehyde for 10 min followed by treatment with ice-cold methanol for 10 min at −20°C. Fixed gonads were washed thrice with PBS-Tween (0.25% Tween in 1X PBS) and incubated with blocking buffer (1% BSA, 0.1% Tween and 30mM glycine in 1X PBS) for 1 h at room temperature. After blocking, gonads were incubated in 50μL of primary mouse anti-FLAG antibody (Sigma M2, 1:1000) overnight at 4°C. Next day, gonads were washed thrice with 1X PBS and incubated in secondary Alexa Fluor 488-conjugated goat anti-mouse IgG (Abcam, Cat # ab150113, 1:400) for 2 h at room temperature. Stained gonads were washed thrice for 10 min with 1X PBS. The final wash was carried out with 1:1000 dilution of DAPI (4′,6-diamidino-2-phenylindole dihydrochloride) in 1X PBS to visualize the nuclei. Washing of the gonads was repeated two times with 1X PBS. Gonads were then mounted on 3% agarose pad with a few microliters of Vectashield mounting medium (Vector Laboratories, H-1200) for imaging.

Fluorescence imaging

Live imaging was carried out with a spinning disk confocal (Yokogawa CSU-W1) on a Nikon Ti2E microscope using a prime 95B sCMOS camera (Photometrics) and Metamorph software (Molecular devices, Sunnyvale, California). Appropriate stage live worms were mounted on a 3% agarose pad placed on a glass slide with 5ul of 10mM levamisole. Fixed and stained gonads were mounted with Vectashield mounting medium (Vector Laboratories, H-1200). To analyze gonad morphology and nucleus displacement, images were acquired using 60X and 100X oil-immersion Plan-Apochromat objective, respectively.

MICROFLUIDIC DEVICE FABRICATION

Microfluidic devices were fabricated as described in Berger et al.[41] Briefly, master molds were fabricated following standard photolithography protocols,[91] using SU8 photoresist (GM1050 and GM1060, Gersteltec) on silicon wafers (Si-Wafer 4P0/>1/525 ± 25/SSP/TTV<10, Siegert Wafer). The fluidic layers of different height (5 and 15 μm for the feeding and worm sections respectively, L2-A device type) were fabricated consecutively on the same wafer, and aligned using a mask aligner (UV-KUB3, Kloe). The master mold for the control layer was fabricated on a separate wafer at a single height of 20 μm. Wafers were treated with chlorotrimethyl silane (Sigma-Aldrich) vapor prior to PDMS casting. PDMS devices were assembled by first spin coating (750 rpm for 30 s) the fluidic wafer with a thin layer of PDMS (Elastosil RT601; ratio 20:1, Wacker). Simultaneously a ∼4 mm thick layer of PDMS (Elastosil RT601; ratio 5:1, Wacker) was cast on the control layer wafer. Both PDMS layers were partially cured at 70°C (15–20 min). Once sufficiently cured the control layer was peeled from the wafer, cut to size and access holes punched (20G Catheter Punch, Syneo). The control layer was then aligned to the fluidic layer using a stereomicroscope. Both layers were thermally bonded to one another overnight at 70°C.[92] Bonded devices were peeled off the wafer, access holes punched (20G Catheter Punch, Syneo) and bonded to cover glass (50 × 24 mm cover glass with selected thickness 0.17 ± 0.01 mm, Hecht Assistant) using an air plasma (Zepto Plasma cleaner, Diener). Fully assembled devices were baked overnight at 70°C to ensure reliable bonding.

Device operation

Microfluidic device were operated as described in Berger et al.[41] First, the on-chip hydraulic valve was filled with deionized water by applying a constant pressure (10–15 psi) to the dead-end valve channel. Second, the device was filled with the bacteria and pressurized to remove all air bubbles from within the device. Finally, worms were introduced via the worm inlet, with animals loaded into the tubing. The tubing was connected to the worm inlet, ensuring that no air was introduced into the system, and worms were pushed into the device by gently applying and releasing pressure on the syringe plunger. Worms were pushed from the common inlet into individual channels of the trap array. All fluidic connections to the device were made using 1/16″ tygon tubing (15157044, Thermo Fisher Scientific), 23G blunt needles (GGA723050, Gonano Dosiertechnik) and 23G hollow steel pins (IP7R23050, Gonano Dosiertechnik), except for the food supply connected were a 1/32″ tygon tubing (15137044, Thermo Fisher Scientific) and 30G blunt

Please cite this article in press as: Agarwal et al., Active nuclear positioning and actomyosin contractility maintain leader cell integrity during gonadogenesis, Current Biology (2024), https://doi.org/10.1016/j.cub.2024.03.049

needles (IP730050, Gonano Dosiertechnik) was used. Both worm and food supply tubing were connected to 1mL syringes, and the general outlet to a waste container. Bacteria food was supplied at a flow rate of 1 μL/h, with an increase in flow rate to 100 μL/h for 15 s every 30 min, to remove possibly accumulated debris (Aladdin AL-1000, WPI). All worm loading was monitored at 10X magnification. Once channels were filled and suitable worms identified within the trap array, a high magnification, high NA objective was focused onto the device and image acquisition started.

On-chip RNAi

L1 stage worms were initially grown on RNAi plates (prepared using the method described in RNA interference section) for 24 h and then, harvested and loaded into the microfluidic device as described above.

Worms on-chip were fed the RNAi bacteria (empty vector, or *unc-83*;*nmy-2(*RNAi)). Bacteria food was prepared starting with 20 mL overnight culture in LB medium supplemented with ampicillin (0.1 mg/mL), followed by addition of 20mL LB medium supplemented with IPTG (1 mM) and ampicillin (0.1 mg/mL) to induce dsRNA synthesis. The saturated bacterial cultures was pelleted by centrifugation (3000 g for 2 min) and washed with fresh S-Basal buffer for a total of three washes. Note: For double RNAi experiments (*unc-83*; *nmy-2*(RNAi)), half the volume was prepared for each RNAi condition, processed as described and combined prior to the final washing step. Finally, bacteria were pelleted and re-suspended in 1 mL fresh S-Basal, and 1 mL of bacterial suspension was mixed with 0.59 mL Optiprep (Sigma-Aldrich) for density matching of bacteria in suspension, 0.39 mL S-Basal supplemented with 1wt% Pluronic F127 (Sigma-Aldrich) and an additional 0.002 mL of IPTG (1 M stock concentration). Before filling the device, the bacteria suspension was passed through a 10 μm filter (pluriStrainer Mini 10 μm, PluriSelect) to remove any large aggregates or debris. Bacteria food was prepared fresh for every experiment.

All images on-chip were acquired using a spinning disk confocal (Yokogawa CSU-W1) on a Nikon Ti2E microscope using a prime 95B sCMOS camera (Photometrics) and Metamorph software (Molecular devices, Sunnyvale, California). Images were acquired using a 60X oil immersion lens in two colors at a z-spacing of 0.5 μm and a time interval of 15 min for up to 24 h. Image acquisition as well as actuation of the on-chip hydraulic valve (10–15 psi, activated from 10s before until end of image acquisition) was controlled through a custom-built module on Metamorph software. All images were acquired at 20 ± 0.5°C, with temperature control achieved via the room air-conditioning system.

Image analysis

In Figures 1E and 5B, the distance between the nucleus and the DTC front was measured using FIJI software.[85] The distance was calculated by measuring the length of a straight-line drawn between the front edge of the nucleus and the DTC front, as shown in the schematics along with the graphs. For fluorescent intensity measurements, background intensity was quantified at a region outside the worm and subtracted from the whole image. In Figures 1G, S1E and S1I, the average intensity of ANC-1::GFP, UNC-83::GFP::KASH and UNC-84::GFP, respectively, was measured by drawing a 3-pixel circle around the nucleus periphery. In Figures S2C and S4C, the average intensity of NMY-2::mKate and INA-1::mNG was quantified in the entire DTC. In Figure 3E, average fluorescent intensity of FLAG::SYGL-1in the nucleated and enucleated arm was quantified by measuring the mean intensity at three distinct regions near the DTC, and then the ratio of intensity between them was calculated and plotted in the graph (Figure 3F). For Figure 4C, EBP-2::mKate2 comets were detected, tracked in time and their growth length and rate calculated using the spot detection tool in the Imaris software (Oxford Instruments). For Figure 6B, perimeter and aspect ratio under different conditions were measured by FIJI software after thresholding the maximum intensity projected images of the DTC membrane marker (as shown in the right panel of Figure 6A). The curvature of the DTC edge contour was calculated from microscopy images using a custom MATLAB script. The script performs binarization and morphological skeletonization of the raw images using functions from the MATLAB Image Processing Toolbox. The local curvature of the resulting skeleton images was calculated by an adaptation of the curvature detection algorithm presented in Driscoll et al.[93]

Laser ablation

Laser ablation experiments were carried out using an iLAS Pulse system (GATACA Systems). It is equipped with a 355nm laser with an average of 16mW power output. The laser was pulsed at 20Khz frequency with 0.5ns pulse width. L4 stage worms expressing a basement membrane marker, laminin-1::Dendra, were first immobilized using 10mM levamisole and then mounted on a 3% agarose pad placed on a glass slide. A small circular incision was performed using 80% laser power with 20 repetitions at the basement membrane near the distal end of the enucleated DTC of the *unc-83;nmy-2* (RNAi) worms. Subsequently, images were acquired every 1 s for a total duration of 10 s.

QUANTIFICATION AND STATISTICAL ANALYSIS

Prism 9 (GraphPad) and Imaris 8.4.1 (Oxford Instruments) software were used for statistical analysis. Comparison between two samples was done using Student's t-test or Mann Whitney U-test. One-way ANOVA analysis was used when comparing more than two samples. Data are represented as mean ± sem. Sample numbers are indicated in the figure legends or the main text, and a minimum of three or four independent repeats were conducted for each experiment.

Current Biology, Volume *34*

Supplemental Information

Active nuclear positioning and actomyosin contractility maintain leader cell integrity during gonadogenesis

Priti Agarwal, Simon Berger, Tom Shemesh, and Ronen Zaidel-Bar

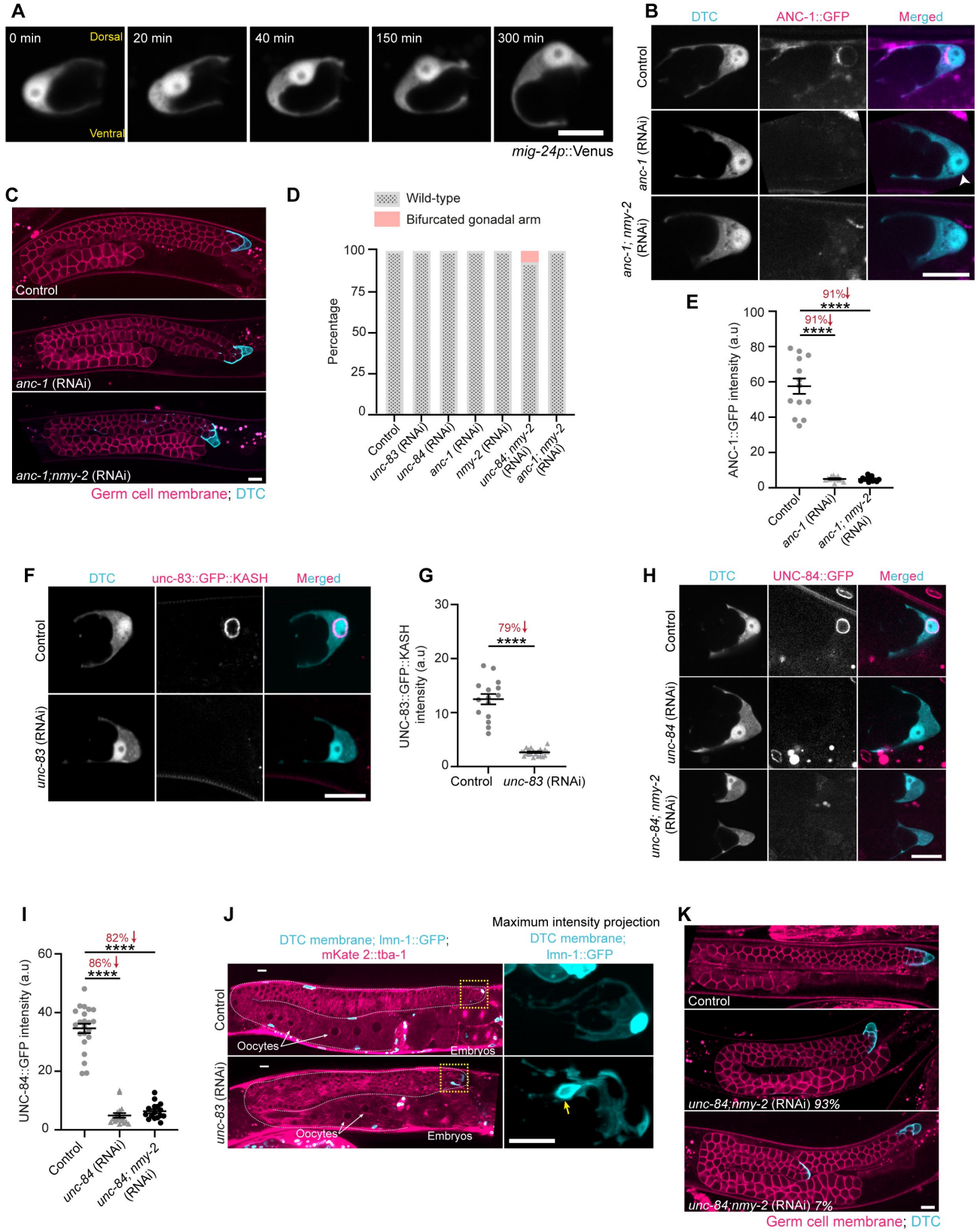
A
0 min
Dorsal
Ventral
20 min
40 min
150 min
300 min
mig-24p::Venus
B
DTC
ANC-1::GFP
Merged
Control
anc-1 (RNAi)
anc-1; nmy-2 (RNAi)
C
Control
anc-1 (RNAi)
anc-1;nmy-2 (RNAi)
Germ cell membrane; DTC
D
Wild-type
Bifurcated gonadal arm
Percentage
100
75
50
25
0
Control
unc-83 (RNAi)
unc-84 (RNAi)
anc-1 (RNAi)
nmy-2 (RNAi)
unc-84; nmy-2 (RNAi)
anc-1; nmy-2 (RNAi)
E
ANC-1::GFP intensity (a.u)
91%↓
****
91%↓
****
100
80
60
40
20
0
Control
anc-1 (RNAi)
anc-1; nmy-2 (RNAi)
F
DTC
unc-83::GFP::KASH
Merged
Control
unc-83 (RNAi)
G
UNC-83::GFP::KASH intensity (a.u)
79%↓
****
30
20
10
0
Control
unc-83 (RNAi)
H
DTC
UNC-84::GFP
Merged
Control
unc-84 (RNAi)
unc-84; nmy-2 (RNAi)
I
UNC-84::GFP intensity (a.u)
82%↓
****
86%↓
****
60
40
20
0
Control
unc-84 (RNAi)
unc-84; nmy-2 (RNAi)
J
DTC membrane; lmn-1::GFP; mKate 2::tba-1
Maximum intensity projection
DTC membrane; lmn-1::GFP
Control
unc-83 (RNAi)
Oocytes
Embryos
Oocytes
Embryos
K
Control
unc-84;nmy-2 (RNAi) 93%
unc-84;nmy-2 (RNAi) 7%
Germ cell membrane; DTC

Figure S1. DTC-specific depletion of UNC-83, ANC-1, or UNC-84 does not affect gonad morphogenesis. Related to Figure 1 and 2.

(**A**) Time-lapse fluorescent images of the DTC, expressing *mig-24p*::Venus, showing the frontal nuclear position during the turn. Scale bar, 10µm. (**B**) Confocal images of DTCs expressing ANC-1::GFP (cyan) and a DTC marker (*mig-24p*::WrmScarlet, pink) in control versus *anc-1*(RNAi) and *anc-1;nmy-2*(RNAi) worms. White arrowhead indicates the DTC nuclear position. (**C**) Representative confocal cross section images of gonads expressing a germ cell membrane marker (*pie-1*::mCherry::PH, pink) and a DTC membrane marker (*lag-2*p::mNG::PH, cyan) in control (N = 30) versus *anc-1*(RNAi) (N = 40) and *anc-1;nmy-2*(RNAi) (N = 45) worms. (**D**) Percentage of gonad morphology defects observed in the different knockdown conditions. (**E**) Quantification of ANC-1::GFP intensity at the DTC nucleus periphery in control (N = 13) versus *anc-1*(RNAi) (N = 13) and *anc-1;nmy-2*(RNAi) worms (N = 13). (**F**) Representative images of DTCs expressing UNC-83::GFP::KASH (cyan) and DTC marker (*mig-24p*::WrmScarlet, pink) in control versus *unc-83*(RNAi) worms. (**G)** Quantification of UNC-83::GFP::KASH intensity at the DTC nucleus periphery in control (N = 15) versus *unc-83*(RNAi) worms (N = 22). (**H**) Representative images of the DTC expressing UNC-84::GFP (cyan) and DTC marker (*mig-24p*::WrmScarlet, pink) in control versus *unc-84*(RNAi) and *unc-84;nmy-2*(RNAi) worms. (**I**) Quantification of UNC-84::GFP intensity at the DTC nucleus periphery in control (N = 22) versus *unc-84*(RNAi) (N = 18) and *unc-84;nmy-2*(RNAi) worms (N = 16). (**J**) Representative images of gonads expressing a germ cell membrane marker (*pie-1*::mCherry::PH, pink) and a DTC membrane marker (*lag-2p*::mNG::PH, cyan) in control (n=21) versus *unc-83*(RNAi) adult stage worms (N = 18). Magnified insets on the right display the maximum intensity projected view of the DTC membrane morphology. The nucleus is indicated by a yellow arrow. (**K**) Representative images showing the morphology of a gonad expressing a germ cell membrane marker (*pie-1*::mCherry::PH, pink) and a DTC membrane marker (*lag-2*p::mNG::PH, cyan) in control (N = 37) versus *unc-84; nmy-2*(RNAi) (N = 80) worms. Two phenotypes are shown along with their penetrance. Percentage of depletion of the respective proteins are indicated in each graph in red. Statistical analysis was carried out using One-way ANOVA analysis (C and H) and Mann–Whitney U-tests (F). **** indicates p value < 0.0001. Scale bar, 10µm.

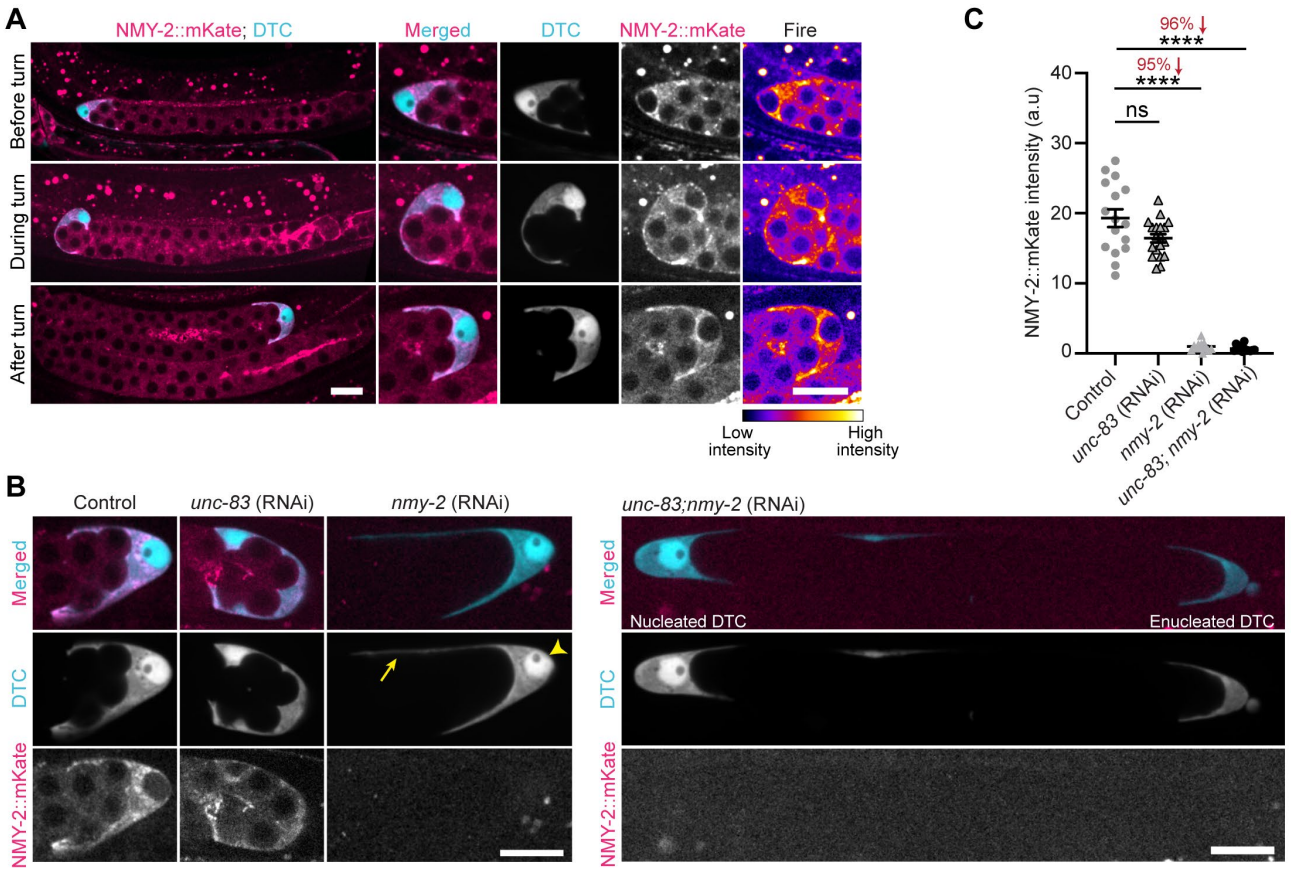

Figure S2. Depletion of non-muscle myosin-II, NMY-2, results in long DTC membrane extensions, but does not affect nuclear positioning within the DTC. Related to Figure 2.
(**A**) Representative images of the gonads expressing NMY-2::mKate, and a DTC marker, *lag-2p*::GFP before, during and after the DTC turn. Magnified insets on the right show NMY-2::mKate distribution within the DTC during different stages. Rightmost panel display the corresponding fire look-up table images. (**B**) Representative images of the DTC expressing NMY-2::mKate, and a DTC marker, *lag-2p*::GFP in control versus *unc-83*(RNAi), *nmy-2*(RNAi) and *unc-83;nmy-2*(RNAi) worms. Yellow arrowhead indicated the position of the DTC nucleus and yellow arrow points towards the long membrane extensions. (**C**) Quantification of NMY-2::mKate intensity within the DTC in control (N = 16) versus *unc-83*(RNAi) (N =19), *nmy-2*(RNAi) (N =12) and *unc-83;nmy-2*(RNAi) (N = 12) worms. Percentage of depletion of NMY-2::mKate intensity in each genotype is indicated in the graph in red. Statistical analysis was carried out using One-way ANOVA analysis. **** indicates p value < 0.0001, ns, non-significant. Scale bar, 10µm.

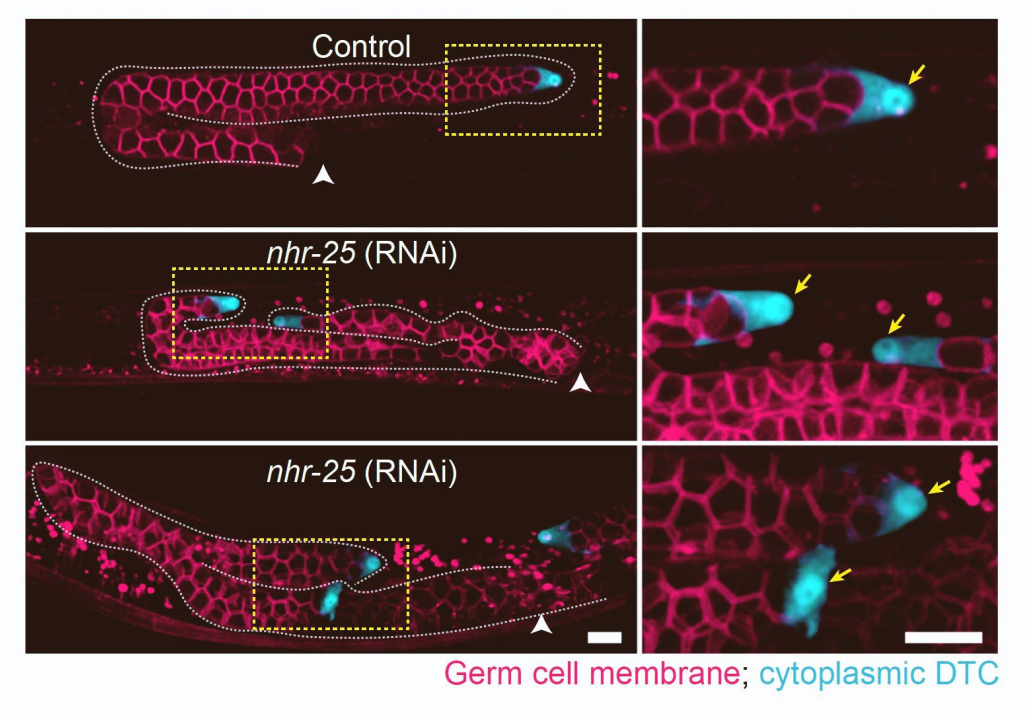

Figure S3. Ectopic DTCs formed after the depletion of NHR-25, a nuclear hormone receptor, possess nuclei. Related to Figure 2. Representative images of gonads expressing a germ cell membrane marker, mCherry::PLC1δ-PH, and a DTC marker, *lag-2p*::GFP. Top panel shows the image of a control gonad, while middle and bottom panels show two different examples of *nhr-25* (RNAi) gonads. The right panel shows magnified images of the DTCs, and yellow arrows point to nuclei. White arrowhead indicates proximal end of the gonad. Scale bars, 10μm.

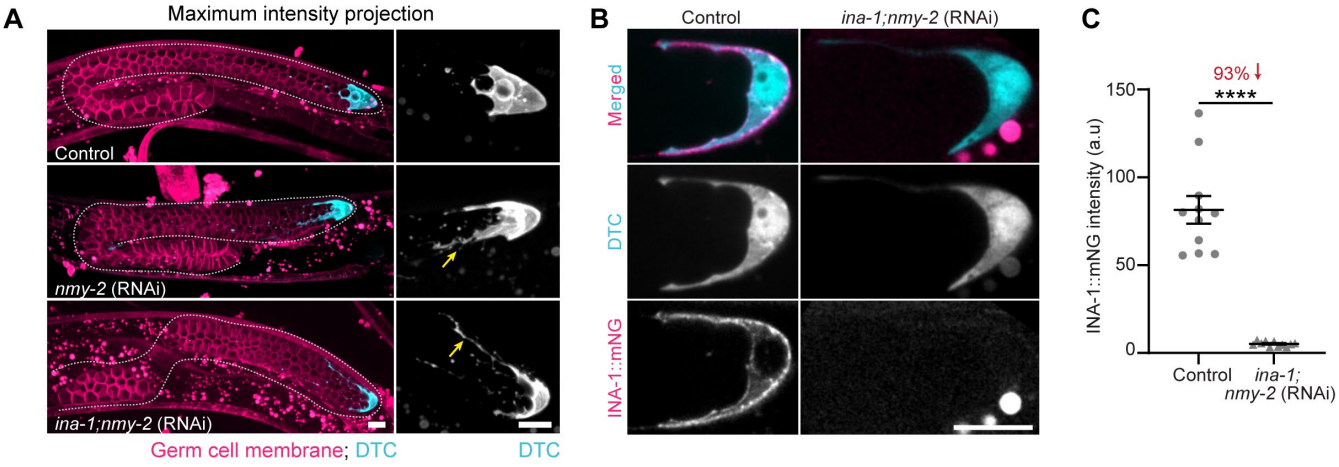

Figure S4. Depletion of the α-integrin, INA-1, does not prevent the formation of long DTC membrane extensions formed in the absence of NMY-2. Related to Figure 2.

(A) Representative maximum Z-projections showing the morphology of a gonad expressing a germ cell membrane marker (*pie-1*::mCherry::PH, pink) and a DTC membrane marker (*lag-2*p::mNG::PH, cyan) in control (N = 23) versus *nmy-2*(RNAi) (N = 24) and *ina-1;nmy-2*(RNAi) (N = 35) worms. Yellow arrows indicate the long DTC membrane extensions. (B) Representative images of the DTC expressing INA-1::mNG, and a DTC marker (*mig-24p*::WrmScarlet, cyan) in control versus *ina-1; nmy-2*(RNAi) worms. (C) Quantification of INA-1::mNG intensity in the DTC in control (N = 11) versus *ina-1;nmy-2*(RNAi) worms (N = 11). Percentage of depletion of INA-1::mNG intensity is indicated in the graph in red. Statistical analysis was carried out using Mann Whitney U-test. **** indicates p value < 0.0001. Scale bar, 10µm.

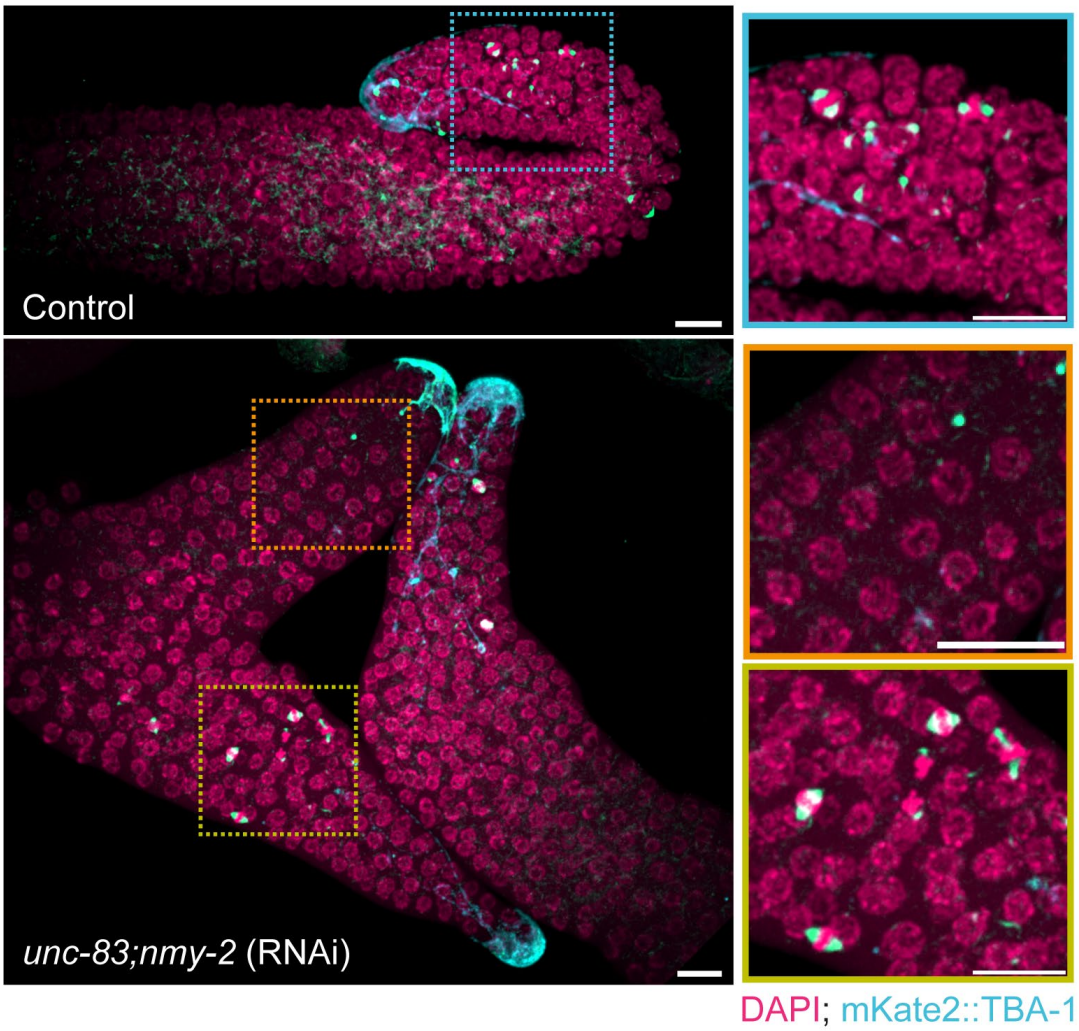

Figure S5. Gonadal arm lead by enucleated DTC lacks mitotically proliferating germ cells in the adult. Related to Figure 3.

Representative images of DAPI stained gonads expressing a DTC membrane marker (*lag-2p*::mNG::PH, cyan) and microtubule marker (mKate2::TBA-1, green) in control versus DTC-specific unc-83;*nmy-2*(RNAi) in adult stage worms. Magnified regions show the mitotically dividing metaphase stage germ cell nuclei (topmost, blue box, and bottommost panel, green box). Middle panel depicts a magnified region of the enucleated arm without any dividing germ cells (orange box). Scale bars, 10µm.

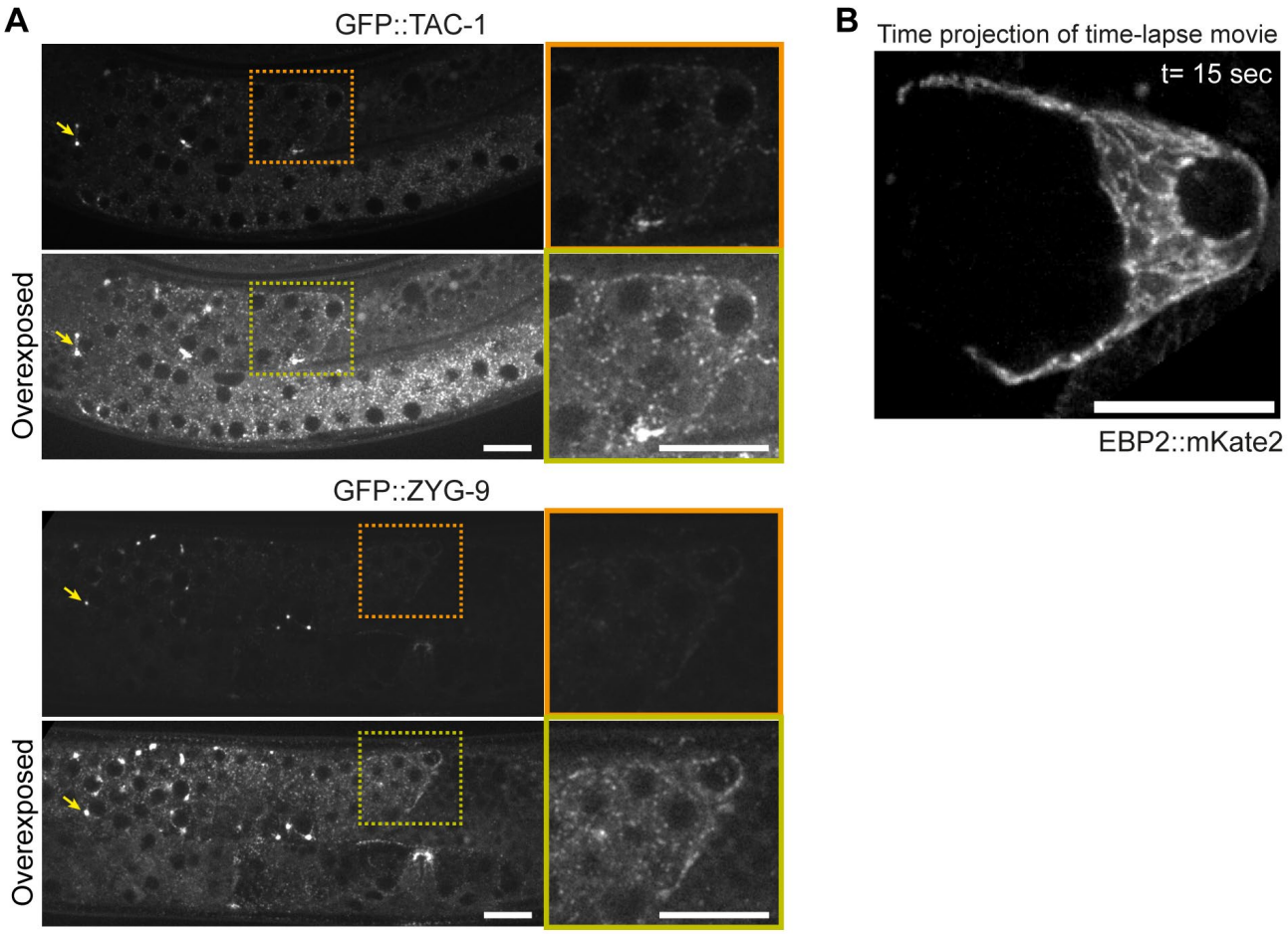

Figure S6. Distal tip cells have acentrosomal microtubules. Related to Figure 4.
(**A**) Representative images of a DTC expressing endogenously GFP-tagged centrosome markers, GFP::TAC-1 and GFP::ZYG-9. Top panel images are shown with normal exposure while the bottom panel shows overexposed images of the same DTCs. Yellow arrows point toward the centrosomes of the dividing germ cells. (**B**) Time projection view of a time lapse movie of EBP-2::mKate2 comets. Images were acquired at 200 msec intervals for a period of 15 seconds. Scale bar is 10µm.

Targeted gene combinations	Number of worms analyzed
nmy-2; cyk-1	20
nmy-2; arx-2	25
nmy-2; wve-1	25
nmy-2; wsp-1	20
nmy-2; cgef-1	23
nmy-2; act-4	20
nmy-2; fln-2	20
nmy-2; unc-83	30
nmy-2; unc-84	24
nmy-2; anc-1	27
nmy-2; lmn-1	20
unc-83; cyk-1	23
unc-83; arx-2	25

Table S1. Double RNAi combinations used for screening defects in gonad morphogenesis. Related to Figure 2.